

Study on the Migrating Speed of Free Alternate Bars

Michihide Ishihara¹, Hiroyasu Yasuda²

¹Graduate School of Science and Technology, Niigata University, Niigata, Japan

²Research Institute for Natural Hazards & Disaster Recovery Niigata University, Niigata, Japan

Key Points:

- The spatial distribution of the migrating speed of alternate bars that occur in rivers was determined.
- A hyperbolic partial differential equation for the bed level and a migrating speed formula were derived.
- The main dominant physical quantity of the migrating speed of alternate bars is the energy slope.

Corresponding author: Hiroyasu Yasuda, hiro@gs.niigata-u.ac.jp

Abstract

In this study, flume experiments were conducted under conditions where alternate bars occur, develop, and migrate, to understand the existence and scale of the spatial distribution of the migrating speed of alternate bars and their dominant physical quantities. In the flume experiment, the bed level and water level during the development of alternate bars were measured with high frequency and high spatial resolution. By comparing the geometric variation of the bed shape, the results showed that the migrating speed of the alternate bars is spatially distributed and changes with time. Next, to quantify the spatial distribution of the migrating speed of the alternate bars, a hyperbolic partial differential equation for the bed level and the calculating equation of the migrating speed based on the advection term of the same equation were derived. Subsequently, the derived equation was shown to be applicable by comparing it with the measurements obtained in the flume experiments described above. The migrating speed of the alternate bars was calculated using above formulas, and it was found to have a spatial distribution that changed with the development of the alternate bars over time. The mathematical structure of the equation showed that the three dominant physical quantities of the migrating speed are the particle size, Shields number, and energy slope. In addition, our method is generally applicable to actual rivers, where the scale and hydraulic conditions are different from those in the flume experiments.

Plain Language Summary

Periodic river bed undulations, called alternate bars are spontaneously formed in rivers, which are located at sites from the alluvial fan to the natural embankment. The physical properties of these alternate bars are known to shift phases in a similar manner to water surface waves during floods. However, there is still a lack of understanding of the migrating speed of alternate bars. We first conducted a flume experiment under the condition that alternate bars can occur and develop. We measured the hydraulic quantity and bed shape using a high spatial resolution. Next, we quantified the migrating speed of the alternate bars using the measured values and the authors's model. This study determined that the migrating speed of the alternate bars has a spatial distribution, and it changes with time. Furthermore, the authors applied authors's model to a actual river during a flood event, and showed that it can provide good estimates of the migrating speed of alternate bars. This study will contribute to the systematic maintenance of river channels where the development and migration of bars are significant.

1 Introduction

Periodic forms can spontaneously occur along the surface of a river channel bed. These forms are called riverbed waves because of their geometrical shapes and physical properties. Riverbed waves can be classified as small-scale, mesoscale, and large-scale, depending on the spatial scales, which include the wavelength and wave height (Seminara, 2010). Small-scale riverbed waves have wavelengths on the scale of the water depth, whereas mesoscale riverbed waves have wavelengths on the river width scale and wave heights on the water depth scale. Large-scale riverbed waves have larger scales. The target of this study was the alternate bars that correspond to mesoscale riverbed waves. Alternate bars are riverbed waves that are spontaneously formed in rivers and are located at sites from the alluvial fan to the natural embankment. When observing alternate bars from the sky using aerial photographs (Fig. 1(a)), the tip part is diagonally connected to the left and right riverbanks; a deep-water pool is located downstream of this tip. Alternate bars can be broadly classified into two categories: 1) free bars, which occur naturally in straight chan-

62 nels owing to the instability of the bottom surface, and 2) forced bars, which occur
63 because of forcing derived from the channel's planar shape and boundary conditions
64 (Seminara, 2010). In this study, among the above categories, free alternate bars are
65 targeted. Because of the physical properties of these alternate bars, their phases are
66 changed in a similar manner to water surface waves during floods of a magnitude
67 that causes active sediment transport (Fig. 1(a),(b)).

68 Over the years, numerous studies have been conducted on alternate bars. One
69 of the initial studies consisted of flume experiments that were performed by Kinoshita
70 (1961). Kinoshita conducted long-term flume experiments to understand the dy-
71 namics of alternate bars that can produce meandering streams. He reported that
72 1) alternate bars have a globally uniform migrating speed and wavelength, 2) al-
73 ternate bars in the early stages of development have short wavelengths and fast
74 migrating speeds, and 3) the migrating speed becomes slower with the growth of
75 wavelengths. These results have been confirmed in subsequent studies (Fujita & Mu-
76 ramoto, 1982; Ikeda, 1983; Fujita & Muramoto, 1985; Nagata et al., 1999). In ad-
77 dition to the aforementioned conclusions, a formula was proposed to calculate the
78 migrating speed of alternate bars based on experimental results, with the Froude
79 number and shear velocity as the dominant physical quantities. However, the valid-
80 ity of this formula was not demonstrated in the same study.

81 In addition to studies using flume experiments, several studies have applied
82 mathematical analyses to understand the mechanism of development of alternate
83 bars. The first mathematical study on alternate bars was conducted by Callander
84 (1969), who extended the instability analysis proposed by Kennedy (Kennedy, 1963)
85 for small-scale bed waves to a two-dimensional plane problem, and theoretically
86 discussed the physical quantities that govern the generation of mesoscale riverbed
87 waves. This study led to a unified study on the generation mechanism of small-
88 scale and meso-scale riverbed waves using instability analysis with the introduction
89 of a lag distance (Hayashi et al., 1982; Ozaki & Hayashi, 1983). After that, stud-
90 ies aimed at predicting the conditions for the occurrence of alternate bars and the
91 wavelength and wave height after their development have been conducted (Kuroki
92 & Kishi, 1984; Colombini et al., 1987; Colombini & Tubino, 1991; Tubino, 1991;
93 Schielen et al., 1993; Izumi & Pornprommin, 2002; Bertagni & Camporeale, 2018).
94 In these instability analyses, an equation for calculating the migrating speed of small
95 bed perturbation was derived during analysis. Kuroki and Kishi (1984) et al. com-
96 pared the calculated and measured values of the migrating speed and reported that
97 the calculated value reproduced the measured value well. The calculated value is
98 the migrating speed at the wavenumber of the maximum amplification rate, and the
99 measured value is calculated from the time variation of the position of the tip of the
100 bar. However, because the migrating speed obtained from the analysis corresponds
101 to the wave number, its spatial distribution has neither been calculated nor deter-
102 mined from measurements.

103 With the emergence of instability analysis, numerical analyses of riverbed fluctu-
104 ations during the occurrence and development of alternate bars began. Shimizu
105 and Itakura (1989) reported for the first time that numerical analysis can satisfac-
106 torily reproduce each process of the occurrence and development of alternate bars.
107 Recently, Federici and Seminara (2003) reported the propagation direction of small-
108 bed perturbation by performing instability and numerical analyses.

109 Other studies using flume experiments (Lanzoni, 2000a, 2000b; Miwa et al.,
110 2007; Crosato et al., 2011, 2012; Venditti et al., 2012; Podolak & Wilcock, 2013)
111 have investigated the effects of external factors, such as the amount of sediment
112 supply and flow discharge, on the dynamics of alternate bars. Crosato et al. (2011,
113 2012) reported that alternate bars eventually shift from being migrating bars to
114 steady bars; they performed flume experiments and a numerical analysis to verify

115 this. Next, Venditti et al. (2012) reported that when sediment supply was inter-
 116 rupted after alternate bars occurred, the bed slope and Shields number decreased,
 117 and the bars disappeared accordingly. Podolak and Wilcock (2013) studied the re-
 118 sponse of alternate bars to sediment supply by increasing the sediment supply dur-
 119 ing the occurrence and development of alternate bars. A non-migrating bar changed
 120 to a migrating bar with an increase in the bed slope and Shields number because of
 121 the increase in the sediment supply. This result from Podolak et al. was followed up
 122 in a subsequent study (Nelson & Morgan, 2018).

123 Several studies have also been conducted on real rivers (Eekhout et al., 2013;
 124 Adami et al., 2016). Eekhout et al. (2013) investigated the dynamics of alternate
 125 bars in rivers for nearly three years and reported that the migrating speed decreased
 126 as the wavelength and wave height of alternate bars increased and the bed slope de-
 127 creased. In addition, Adami et al. (2016) studied the behavior of alternate bars in
 128 the Alps and Rhine River over several decades. They established the relationship be-
 129 tween the flow discharge and migrating speed of bars and confirmed that bars move
 130 less when the flow rate is very high and move significantly when the flow discharge is
 131 in the middle scale of the flow discharge.

132 Through previous studies, predicting the occurrence and geometry of alternate
 133 bars has become possible to some extent. In contrast, an understanding of the na-
 134 ture of the migrating speed of alternate bars is still lacking. In this study, consid-
 135 ering the physics of alternate bars, which has not yet been fully demonstrated, we
 136 focused on the migrating speed and conducted the following experiments to clarify
 137 the dominant physical quantities, and the existence and scale of their spatial dis-
 138 tribution and migrating speed. In Section 2, we describe the outline of the flume
 139 experiment using stream tomography (ST), which can simultaneously measure the
 140 geometric shapes of the water and bed surfaces with a high spatial resolution, and
 141 the measurement results. In Section 3, we assume that the alternate bars can be re-
 142 garded as a wave phenomenon, and we derive a hyperbolic partial differential equa-
 143 tion (HPDE) for the bed level. In this study, the advection velocity given to the ad-
 144 vection term of the HPDE was used to calculate the migrating speed of the alternate
 145 bars. In Section 4, the validity of the calculation formula derived in Section 3 is ver-
 146 ified based on the characteristics of the HPDE and the measured values of the bed
 147 level obtained in Section 2. In Section 5, the spatial distribution of the migrating
 148 speed of the alternate bars is quantified using the formula to calculate the migrating
 149 speed. In Section 6, the applicability of the above formula to real rivers is discussed.
 150 Section 7 describes the results obtained in Section 5, and Section 8 summarizes the
 151 research results.

152 **2 Quantification of the Propagation Phenomenon in Alternate Bars** 153 **Based on the Flume Experiment**

154 **2.1 Experimental Setup**

155 Figure 2 shows a plan view of the experiment flume. The experimental channel
 156 consisted of a flume channel with a straight rectangular cross section. The flume had
 157 a length of 12.0 m, width of 0.45 m, and depth of 0.15 m. Fixed weirs with the same
 158 width as the flume were located 2.7 m from the upstream and downstream ends of
 159 the flume. Over the section 2.7–9.3 m from the upstream end that was sandwiched
 160 by these weirs, the initial bed of the channel for the experiment was a set flat bed.
 161 The bed was fabricated from a non-cohesive material with a mean diameter of 0.76
 162 mm and the bed thickness was 5.0 cm.

163 For water supply to the channel, circulation-type pumping from a water tank
 164 at the downstream end to a water tank at the upstream end was adopted; water was

165 steadily supplied. The accuracy of the water discharge was confirmed using an elec-
166 tromagnetic flowmeter.

167 2.2 Experimental Condition

168 The purpose of this study is to understand the dominant physical quantities of
169 the migrating speed of the alternate bars and the existence and scale of their spa-
170 tial distribution. In the following experiment, we set up the hydraulic conditions un-
171 der which alternate bars are expected to develop and migrate. It has been theoret-
172 ically shown that the occurrence of alternate bars can be estimated using the river
173 width–depth ratio (Callander, 1969; Kuroki & Kishi, 1984). Kuroki and Kishi (1984)
174 showed that the type of bars occurred can be classified based on $BI_0^{0.2}/h_0$, which is
175 the bed slope I_0 added to the river width–depth ratio β . In this study, we set two
176 conditions that correspond to the area of occurrence of alternate bars, as shown in
Table. 1.

Table 1. Experimental condition.

Case	Flow discharge [L/s]	width [m]	slope	h_0 [m]	$BI_0^{0.2}/h_0$	β	τ_*
1	2.0	0.45	1/160	0.014	11.4	31.45	0.0713
2	2.6	0.45	1/200	0.018	8.7	25.13	0.0714

177

178 The validity of the formula was verified by comparing the calculated values of
179 the migrating speed of the instability analysis and the calculated values of the mi-
180 grating speed derived in this study. Therefore, based on the characteristics of insta-
181 bility analysis, the conditions were set such that the particle size and Shields number
182 were fixed, and the river width–depth ratio became a variable. The same experiment
183 was conducted twice for each condition to confirm the reproducibility of the results.

184 These experimental conditions exceed the critical Shields number of 0.034 ob-
185 tained from equation of Iwagaki (1956). The sediment supply condition at the up-
186 stream end was set to no supply. The no-supply condition was chosen because pre-
187 liminary experiments comparing the effects of the presence and absence of sediment
188 supply on the spatial distribution of the migrating speed of alternate bars and its
189 temporal variation showed that the spatial distribution of the migrating speed was
190 more likely to expand in the no-supply condition.

191 Water flow was carried out for 2 h during this experiment with the aforemen-
192 tioned conditions. At this time, alternate bars developed, and their propagation and
193 shape change became slow.

194 2.3 Measurement Method for the Bed Surface and Water Surface

195 In this study, we used Stream Tomography (ST), which was developed by Hoshino
196 et al. (2018), to measure the bed and water levels in a plane while the water was
197 flowing. For details on the principles of the ST measurement, refer to Appendix
198 A. In this study, the aforementioned measurements were performed with a spatial
199 resolution of 2 cm² for every minute. The water depth was calculated from the dif-
200 ference between the water level and bed level. Because the ST measurements were
201 missing near the side walls, the data of 0.38-m width excluding the side walls were
202 used.

2.4 Measurement Results

In this section, we describe the migration phenomena of alternate bars based on high-resolution spatial measurements by the ST, using a plan view of the basal level of Fig. 3 and a longitudinal section of Fig. 4. The same figures show the measurement results of Condition 2, where typical alternate bars were formed. The results of the other condition differed from those of Condition 2 only in terms of the wavelength and wave height, but no essential difference was observed. For the results of the other condition, please refer to the database (Ishihara & Yasuda, 2022).

Figure 3 shows the plan view of the deviation of the bed level by ST. The origin of the vertical coordinates of the ST is the flume bottom. Therefore, the water level and bed level represent the height from the bed of the flume. In this study, the initial bed was shaped to be completely flat in the transverse direction as much as possible, but the bed was not completely flat due to the limitation of the shaping jig. The transverse slope of the initial bed may affect the occurrence and development of alternate bars. However, the experimental results shown in Fig. 3 are almost the same as the equilibrium wave height and wavelength obtained by the instability analysis described in Section 7.4 of the Discussion. In addition, the alternate bars occurred and developed were almost identical to the geometrical shapes of alternate bars in previous studies (Kinoshita, 1958; Federici & Seminara, 2003; Crosato et al., 2011; Venditti et al., 2012; Podolak & Wilcock, 2013). These results suggest that the transverse slope of the initial riverbed is not a concern.

First, it can be observed that the bottom shape did not change much from the initial flat bed in Fig. 3 from (a) to (d). Second, the bed topography in which deposition and scouring are alternately repeated in the downstream direction, that is, 2.0 m, 3.0 m, and 5.0 m from the upstream end, can be observed; thus, it can be confirmed that alternate bars occurred (Fig. 3(e)). In this study, we defined (e) 40 min, in which the geometric features of the alternate bars were confirmed from the measured result by the ST, as the occurrence time of the alternate bars. The alternate bars develop undulations with time, becoming more sedimented in the sedimented areas and more scoured in the scoured areas, which indicates that the entire bar is gradually migrating downstream. A series of observations from (g) 60 min to (m) 120 min of water flow shows that bars are migrating at a constant speed.

Next, Figure 4 shows the longitudinal distribution of the deviation in the bed level on the green dotted line in Fig. 3. Figure 4 shows (a) the initial stage of the experiment, (b) the occurrence of alternate bars, (c) the intermediate stage of the experiment, and (d) the final stage of the experiment. Figure 4 shows three results, where each one is 10 min apart. First, the deviation of the bed level was confirmed to maintain a nearly flat bed from 1 min to 20 min (Fig. 4(a)). After (b) 60 min, three bed undulations developed 2.5 m, 4.5 m, and 5.5 m from the upstream end. The amplitudes of the bed undulations developed, and they migrated in the downstream direction. This undulation migrated downstream with amplification of wave height from (b) 60 to 120 min of water flow. The above results indicate that the waviness of the alternate bars is being measured. In Fig. 4(d), a decrease in the bed level was observed in the upstream section because the experimental conditions were set to no sediment supply. On the other hand, there was no decrease in the bed level in the downstream of the half of the channel even at the time when the water flow was terminated. This suggests that the effect of the no-sediment supply condition did not spread downstream of the half of the channel at the end of the experiment.

The linear wave theory indicates that the phase propagates without deforming the waveform if a wave propagates with a spatial and temporal constant migrating speed. Conversely, in nonlinear wave theory, in which the migrating speed has a spatial distribution and temporal changes, the wave propagates with deformation

255 of the waveform. From the viewpoint of the aforementioned wave theories, the mi-
 256 grating speed of the bars after the occurrence of alternate bars in (b) has a spatial
 257 distribution and is estimated to change with time, and it has the characteristics of a
 258 nonlinear wave.

259 **3 Derivation of the Calculation Formula for the Migrating Speed** 260 **of Alternate Bars**

261 As shown in the previous section, the measurement results of this study show
 262 the nature of the wave in the process of the occurrence and development of alter-
 263 nate bars. These findings are similar to what has been reported in the literature
 264 (Kinoshita, 1958; Federici & Seminara, 2003; Crosato et al., 2011; Venditti et al.,
 265 2012; Podolak & Wilcock, 2013). In other words, there is scope for quantifying the
 266 spatial distribution of the migrating speed by an indirect method using a mathemat-
 267 ical model such as the HPDE (Fujita et al., 1985), which is suitable for describing
 268 the wave phenomena. The formula for calculating the migrating speed is also de-
 269 rived from instability analysis (Callander, 1969; Kuroki & Kishi, 1984). However, be-
 270 cause the formula calculates the migrating speed for each wave number, the spatial
 271 distribution of the migrating speed cannot be quantified. Another possible method is
 272 to set up feature points at the front edge of an alternate bar and to calculate the mi-
 273 grating speed based on the trajectory. However, both methods fail to obtain a con-
 274 tinuous spatial distribution of the migrating speed. In addition, it is not possible to
 275 calculate the migrating speed using numerical analysis of the occurrence and devel-
 276 opment of bars. Therefore, in this study, we derived a hyperbolic partial differential
 277 equation for the bed level and quantified the spatial distribution of the migrating
 278 speed of alternate bars using the advection velocity, which is the coefficient of the
 279 advection term of the HPDE.

280 This section describes the derivation process of the HPDE for bed level z . In
 281 addition, four different formulas were obtained depending on the physical assump-
 282 tions. This includes whether the dimension is one-dimensional or two-dimensional,
 283 and whether the flow is stationary or unsteady. First, regarding the stationarity of
 284 flow, as we confirmed that the non-stationary state in the phenomenon targeted by
 285 this study is very small from the verification results described in Appendix B, we
 286 decided to consider only the stationary state. In terms of dimensions, the geometric
 287 shape of the alternate bars and the flow each have two-dimensional plane character-
 288 istics. Therefore, we aimed to derive a two-dimensional stationary equation.

289 The derivation of the HPDE for the bed level can be used for the continuous
 290 equation of the sediment, sediment functions, and the equation of the water surface
 291 profile. For the derivation, the Exner equation was used as the continuous equation
 292 of the sediment, and the Meyer–Peter and Müller (MPM) formula were used as the
 293 sediment function and two-dimensional equation of the water surface profile, respec-
 294 tively. The application of the HPDE to the various sediment functions was examined
 295 using the method described in the next section. In this study, the MPM formula,
 296 which is simple and has good applicability, was adopted. Vectors for longitudinal
 297 Eq. (2) and transverse Eq. (3) for the sediment flux were assumed based on equa-
 298 tion of Watanabe et al. (2001). Equation (7) was used to calculate the Shields num-
 299 ber. We derived the steady two-dimensional equation of the water surface profile (
 300 Eq. (5), Eq. (6)) to derive the HPDE for the bed level. For details on the deriva-
 301 tion process of the steady two-dimensional equation for the water surface profile,
 302 please refer to Appendix C.

$$\frac{\partial z}{\partial t} + \frac{1}{1 - \lambda} \left(\frac{\partial q_{Bx}}{\partial x} + \frac{\partial q_{By}}{\partial y} \right) = 0 \quad (1)$$

303

$$q_{Bx} = 8(\tau_* - \tau_{*c})^{3/2} \sqrt{sgd^3} \left(\frac{u}{V} - \frac{\gamma'}{\tau_*^{1/2}} \frac{\partial z}{\partial x} \right) \quad (2)$$

304

$$q_{By} = 8(\tau_* - \tau_{*c})^{3/2} \sqrt{sgd^3} \left(\frac{v}{V} - \frac{\gamma'}{\tau_*^{1/2}} \frac{\partial z}{\partial y} \right) \quad (3)$$

305

$$\gamma' = \sqrt{\frac{\tau_{*c}}{\mu_s \mu_k}} \quad (4)$$

306

$$\frac{\partial h}{\partial x} = -\frac{\partial z}{\partial x} - I_{ex} - \frac{3}{5} \frac{u^2}{gI_{ex}} \frac{\partial I_{ex}}{\partial x} + \frac{3}{10} \frac{u^2}{gI_e} \frac{\partial I_e}{\partial x} + \frac{2}{5} \frac{uv}{gI_{ey}} \frac{\partial I_{ey}}{\partial y} + \frac{3}{10} \frac{uv}{gI_e} \frac{\partial I_e}{\partial y} - \frac{uv}{gI_{ex}} \frac{\partial I_{ex}}{\partial y} \quad (5)$$

307

$$\frac{\partial h}{\partial y} = -\frac{\partial z}{\partial y} - I_{ey} - \frac{3}{5} \frac{v^2}{gI_{ey}} \frac{\partial I_{ey}}{\partial y} + \frac{3}{10} \frac{v^2}{gI_e} \frac{\partial I_e}{\partial y} + \frac{2}{5} \frac{uv}{gI_{ex}} \frac{\partial I_{ex}}{\partial x} + \frac{3}{10} \frac{uv}{gI_e} \frac{\partial I_e}{\partial x} - \frac{uv}{gI_{ey}} \frac{\partial I_{ey}}{\partial x} \quad (6)$$

308

$$\tau_* = \frac{hI_e}{sd} \quad (7)$$

309

310

311

312

313

314

315

316

317

318

where z is the bed level, t is the time, λ is the porosity of the bed, q_{Bx} is the longitudinal sediment flux, x is the distance of the longitudinal direction, q_{By} is the transverse sediment flux, y is the distance of the transverse direction, τ_* is the composite Shields number, τ_{*c} is the critical Shields number, s is the specific gravity of sediments in water, g is the acceleration due to gravity, d is the sediment size, u is the longitudinal flow velocity, V is the composite flow velocity, v is the transverse flow velocity, μ_s is the coefficient of static friction, μ_k is the coefficient of dynamic friction, and h is the depth. In addition, $I_{bx} = -\partial z/\partial x$ is the longitudinal bed slope, I_{ex} is the longitudinal energy slope, $I_{by} = -\partial z/\partial y$ is the transverse bed slope, and I_{ey} is the transverse energy slope.

319

320

First, by applying the chain rule of differentiation to $\partial q_{Bx}/\partial x$ in Eq. (1), we can obtain the following, where n is the coefficient of roughness.

$$\begin{aligned} \frac{\partial q_{Bx}}{\partial x} &= \frac{\partial q_{Bx}}{\partial \tau_*} \frac{\partial \tau_*}{\partial x} + \frac{\partial q_{Bx}}{\partial u} \frac{\partial u}{\partial x} + \frac{\partial q_{Bx}}{\partial V} \frac{\partial V}{\partial x} + \frac{\partial q_{Bx}}{\partial(\partial z/\partial x)} \frac{\partial(\partial z/\partial x)}{\partial x} \\ &= \frac{\partial q_{Bx}}{\partial \tau_*} \left(\frac{\partial \tau_*}{\partial h} \frac{\partial h}{\partial x} + \frac{\partial \tau_*}{\partial I_e} \frac{\partial I_e}{\partial x} \right) + \frac{\partial q_{Bx}}{\partial u} \frac{\partial u}{\partial x} + \frac{\partial q_{Bx}}{\partial V} \frac{\partial V}{\partial x} + \frac{\partial q_{Bx}}{\partial(\partial z/\partial x)} \frac{\partial^2 z}{\partial x^2} \\ &= \frac{\partial q_{Bx}}{\partial \tau_*} \left(\frac{I_e}{sd} \frac{\partial h}{\partial x} + \frac{h}{sd} \frac{\partial I_e}{\partial x} \right) + \frac{\partial q_{Bx}}{\partial u} \frac{\partial u}{\partial x} + \frac{\partial q_{Bx}}{\partial V} \frac{\partial V}{\partial x} + \frac{\partial q_{Bx}}{\partial(\partial z/\partial x)} \frac{\partial^2 z}{\partial x^2} \\ &= \frac{\partial q_{Bx}}{\partial \tau_*} \frac{I_e}{sd} \left(\frac{\partial h}{\partial x} + \frac{h}{I_e} \frac{\partial I_e}{\partial x} \right) + \frac{\partial q_{Bx}}{\partial u} \frac{\partial u}{\partial x} + \frac{\partial q_{Bx}}{\partial V} \frac{\partial V}{\partial x} + \frac{\partial q_{Bx}}{\partial(\partial z/\partial x)} \frac{\partial^2 z}{\partial x^2} \end{aligned} \quad (8)$$

321

322

In addition, $\partial I_e/\partial x$ in Eq. (8) becomes the following when the chain rule is applied to differentiate the Manning flow velocity Eq. (9).

$$V = \frac{1}{n} I_e^{1/2} h^{2/3} \quad (9)$$

323

$$\frac{\partial I_e}{\partial x} = \frac{\partial I_e}{\partial h} \frac{\partial h}{\partial x} + \frac{\partial I_e}{\partial V} \frac{\partial V}{\partial x} = -\frac{4}{3} \frac{I_e}{h} \frac{\partial h}{\partial x} + 2 \frac{I_e}{V} \frac{\partial V}{\partial x} \quad (10)$$

324

325

Substituting Eq. (10) in Eq. (8) and rearranging, we can obtain the following equation.

$$\frac{\partial q_{Bx}}{\partial x} = \frac{\partial q_{Bx}}{\partial \tau_*} \frac{I_e}{sd} \left(-\frac{1}{3} \frac{\partial h}{\partial x} + 2 \frac{h}{V} \frac{\partial V}{\partial x} \right) + \frac{\partial q_{Bx}}{\partial u} \frac{\partial u}{\partial x} + \frac{\partial q_{Bx}}{\partial V} \frac{\partial V}{\partial x} + \frac{\partial q_{Bx}}{\partial(\partial z/\partial x)} \frac{\partial^2 z}{\partial x^2} \quad (11)$$

326 $\partial q_{Bx}/\partial\tau_*$, $\partial q_{Bx}/\partial u$, $\partial q_{Bx}/\partial V$, $\partial q_{Bx}/\partial(\partial z/\partial x)$ in the aforementioned equation is
 327 given as follows.

$$\frac{\partial q_{Bx}}{\partial\tau_*} = 8(\tau_* - \tau_{*c})^{1/2} \sqrt{sgd^3} \frac{3}{2} \left[\frac{u}{V} - \frac{\gamma'}{\tau_*^{1/2}} \left\{ 1 - \frac{1}{3\tau_*} (\tau_* - \tau_{*c}) \right\} \frac{\partial z}{\partial x} \right] \quad (12)$$

328

$$\frac{\partial q_{Bx}}{\partial u} = 8(\tau_* - \tau_{*c})^{3/2} \sqrt{sgd^3} \frac{1}{V} \quad (13)$$

329

$$\frac{\partial q_{Bx}}{\partial V} = -8(\tau_* - \tau_{*c})^{3/2} \sqrt{sgd^3} \frac{u}{V^2} \quad (14)$$

330

$$\frac{\partial q_{Bx}}{\partial(\partial z/\partial x)} = -8(\tau_* - \tau_{*c})^{3/2} \sqrt{sgd^3} \frac{\gamma'}{\tau_*^{1/2}} \quad (15)$$

331 Equation (5) is used for $\partial h/\partial x$. Substituting Eq. (5), Eq. (12), Eq. (13), Eq. (14)
 332 and Eq. (15) in Eq. (11), Eq. (11) becomes the following.

$$\begin{aligned} & \frac{\partial q_{Bx}}{\partial x} = 4(\tau_* - \tau_{*c})^{1/2} \sqrt{sgd^3} \frac{I_e}{sd} \left[\frac{u}{V} - \frac{\gamma'}{\tau_*^{1/2}} \left\{ 1 - \frac{1}{3\tau_*} (\tau_* - \tau_{*c}) \right\} \frac{\partial z}{\partial x} \right] \\ & \left\{ \frac{\partial z}{\partial x} + I_{ex} + \frac{3}{5} \frac{u^2}{gI_{ex}} \frac{\partial I_{ex}}{\partial x} - \frac{3}{10} \frac{u^2}{gI_e} \frac{\partial I_e}{\partial x} - \frac{2}{5} \frac{uv}{gI_{ey}} \frac{\partial I_{ey}}{\partial y} - \frac{3}{10} \frac{uv}{gI_e} \frac{\partial I_e}{\partial y} + \frac{uv}{gI_{ex}} \frac{\partial I_{ex}}{\partial y} + 6 \frac{h}{V} \frac{\partial V}{\partial x} \right\} \quad (16) \\ & + 8(\tau_* - \tau_{*c})^{3/2} \sqrt{sgd^3} \frac{1}{V} \frac{\partial u}{\partial x} - 8(\tau_* - \tau_{*c})^{3/2} \sqrt{sgd^3} \frac{u}{V^2} \frac{\partial V}{\partial x} - 8(\tau_* - \tau_{*c})^{3/2} \sqrt{sgd^3} \frac{\gamma'}{\tau_*^{1/2}} \frac{\partial^2 z}{\partial x^2} \end{aligned}$$

333 In addition, $\partial q_{By}/\partial y$ is arranged in the same process as Eq. (16), and the following
 334 equation is obtained.

$$\begin{aligned} & \frac{\partial q_{By}}{\partial y} = 4(\tau_* - \tau_{*c})^{1/2} \sqrt{sgd^3} \frac{I_e}{sd} \left[\frac{v}{V} - \frac{\gamma'}{\tau_*^{1/2}} \left\{ 1 - \frac{1}{3\tau_*} (\tau_* - \tau_{*c}) \right\} \frac{\partial z}{\partial y} \right] \\ & \left\{ \frac{\partial z}{\partial y} + I_{ey} + \frac{3}{5} \frac{v^2}{gI_{ey}} \frac{\partial I_{ey}}{\partial y} - \frac{3}{10} \frac{v^2}{gI_e} \frac{\partial I_e}{\partial y} - \frac{2}{5} \frac{uv}{gI_{ex}} \frac{\partial I_{ex}}{\partial x} - \frac{3}{10} \frac{uv}{gI_e} \frac{\partial I_e}{\partial x} + \frac{uv}{gI_{ey}} \frac{\partial I_{ey}}{\partial y} + 6 \frac{h}{V} \frac{\partial V}{\partial y} \right\} \quad (17) \\ & + 8(\tau_* - \tau_{*c})^{3/2} \sqrt{sgd^3} \frac{1}{V} \frac{\partial v}{\partial y} - 8(\tau_* - \tau_{*c})^{3/2} \sqrt{sgd^3} \frac{v}{V^2} \frac{\partial V}{\partial y} - 8(\tau_* - \tau_{*c})^{3/2} \sqrt{sgd^3} \frac{\gamma'}{\tau_*^{1/2}} \frac{\partial^2 z}{\partial y^2} \end{aligned}$$

335 By substituting Eq. (16) and Eq. (17) in Eq. (1), the following HPDE for bed level
 336 z can be derived. This equation is classified as an advection-diffusion equation be-
 337 cause it includes a diffusion term.

$$\frac{\partial z}{\partial t} + M_x \frac{\partial z}{\partial x} + M_y \frac{\partial z}{\partial y} = D \frac{\partial^2 z}{\partial x^2} + D \frac{\partial^2 z}{\partial y^2} - M_x(I_{ex} + F_x) - M_y(I_{ey} + F_y) - F_{x2} - F_{y2} \quad (18)$$

338 In the aforementioned equation, M_x is the advection velocity of the longitudinal
 339 component of bed level z . It is assumed to be closely related to the migrating speed
 340 of the longitudinal component of the alternate bars, which is the subject of this
 341 study. M_y is the transverse migrating speed of the alternate bars. M_x and M_y are
 342 not velocities of the sediments; they are supposed to be the propagation velocities of
 343 bed level z . M_x and M_y are given as follows.

$$M_x = \frac{4(\tau_* - \tau_{*c})^{1/2} \sqrt{sgd^3} I_e}{sd(1 - \lambda)} \left[\frac{u}{V} - \frac{\gamma'}{\tau_*^{1/2}} \left\{ 1 - \frac{1}{3\tau_*} (\tau_* - \tau_{*c}) \right\} \frac{\partial z}{\partial x} \right] \quad (19)$$

344

$$M_y = \frac{4(\tau_* - \tau_{*c})^{1/2} \sqrt{sgd^3} I_e}{sd(1 - \lambda)} \left[\frac{v}{V} - \frac{\gamma'}{\tau_*^{1/2}} \left\{ 1 - \frac{1}{3\tau_*} (\tau_* - \tau_{*c}) \right\} \frac{\partial z}{\partial y} \right] \quad (20)$$

Eq. (19) and Eq. (20) indicate that the dominant physical quantities of the migrating speed are I_e , τ_* , and d . In addition, diffusion coefficient D , F_x , F_y , F_{x2} and F_{y2} are given as follows.

$$D = \frac{8(\tau_* - \tau_{*c})^{3/2} \sqrt{sgd^3} \gamma'}{1 - \lambda} \tau_*^{1/2} \quad (21)$$

$$F_x = \frac{3}{5} \frac{u^2}{gI_{ex}} \frac{\partial I_{ex}}{\partial x} - \frac{3}{10} \frac{u^2}{gI_e} \frac{\partial I_e}{\partial x} - \frac{2}{5} \frac{uv}{gI_{ey}} \frac{\partial I_{ey}}{\partial y} - \frac{3}{10} \frac{uv}{gI_e} \frac{\partial I_e}{\partial y} + \frac{uv}{gI_{ex}} \frac{\partial I_{ex}}{\partial y} + 6 \frac{h}{V} \frac{\partial V}{\partial x} \quad (22)$$

$$F_y = \frac{3}{5} \frac{v^2}{gI_{ey}} \frac{\partial I_{ey}}{\partial y} - \frac{3}{10} \frac{v^2}{gI_e} \frac{\partial I_e}{\partial y} - \frac{2}{5} \frac{uv}{gI_{ex}} \frac{\partial I_{ex}}{\partial x} - \frac{3}{10} \frac{uv}{gI_e} \frac{\partial I_e}{\partial x} + \frac{uv}{gI_{ey}} \frac{\partial I_{ey}}{\partial x} + 6 \frac{h}{V} \frac{\partial V}{\partial y} \quad (23)$$

$$F_{x2} = \frac{8(\tau_* - \tau_{*c})^{3/2} \sqrt{sgd^3}}{1 - \lambda} \left(\frac{1}{V} \frac{\partial u}{\partial x} - \frac{u}{V^2} \frac{\partial V}{\partial x} \right) \quad (24)$$

$$F_{y2} = \frac{8(\tau_* - \tau_{*c})^{3/2} \sqrt{sgd^3}}{1 - \lambda} \left(\frac{1}{V} \frac{\partial v}{\partial y} - \frac{v}{V^2} \frac{\partial V}{\partial y} \right) \quad (25)$$

4 Verifying the Applications of the HPDE for Bed Level z and the Migrating Speed Formula based on the Measured Values

In this section, we investigate the applicability of the HPDE for bed level z and its calculation formula for the migrating speed derived in the previous section.

4.1 Hydraulics Required to Verify Applicability

This section describes the hydraulic quantities required to verify the applicability of the HPDE and the calculation formula for the migrating speed, as explained in the next section. As demonstrated from the HPDE and the calculation formula for the migrating speed shown in the previous section, the hydraulic quantities required for the verification of the applicability are the water depth, energy slope, and flow velocity. The water depth can be obtained from the bed level and water level measured by the ST. However, the flow velocity and energy slope that are paired with the water depth have not been measured—this measurement is generally difficult. Therefore, we determined the flow velocity and energy slope by performing numerical analyses.

For the numerical analysis, Nays2D, included in iRIC (<http://www.i-ric.org>), which can solve the two-dimensional plane hydraulic analysis, was employed. The analysis was conducted with a bed level that was measured by the ST as a fixed bed. The spacing of the calculation points was 2 cm, the same as the ST resolution, in both the longitudinal and transverse directions. The upstream boundary condition was the flow rate of 1.5 L/s, and the downstream boundary condition was the measured water depth. The roughness coefficients were adjusted at each time point, such that the calculated values of the water depth and the measured values agreed with each other and were given uniformly throughout the section.

The measured values of the water depth are shown in Fig. 5, the difference between the measured and calculated values of water depth is shown in Fig. 6, which is nondimensionalized by measurement Δh_* , and the calculated values of flow velocity are shown in Fig. 7. Of these, Δh_* represents the computational accuracy of the numerical analysis. Considering Δh_* in Fig. 6, Δh_* is generally within 10% for the

entire channel at all times, regardless of the development of alternate bars. All the areas where Δh_* was greater than 20% were in very shallow water.

Because Δh_* is nondimensionalized based on the measured values of water depth, it is assumed that Δh_* in this part was calculated to be large. Therefore, it is difficult to determine the computational accuracy of this part by Δh_* . However, if we focus on the calculated values of flow velocity shown in Fig. 7, we can obtain results that are not unnatural as a phenomenon; thus, we decided to use the calculated values of this part as well. In the next section, the applicability of the derived equations is verified using these hydraulic quantities.

4.2 Verifying the Application of the Time Waveform for the Bed Level and the Riverbed Fluctuation Amount

We verified the applicability of the calculation formula derived in the previous section from two viewpoints. First, can the time waveform of the measured bed level be reproduced? Second, can the riverbed fluctuation amount measured in the entire section be reproduced? The verification results are described in this section.

4.2.1 Bed-level Time Waveform

The verification method that uses the time waveform at the bed level is described here. Using the bed level and water depth measured by ST, and the calculated energy gradient and flow velocity from the hydraulic analysis described in the previous section, the HPDE (18) derived in the previous section was numerically integrated, as follows, to calculate the riverbed fluctuation between Δt .

$$\Delta z_{cal} = \left\{ -M_x \frac{\partial z}{\partial x} - M_y \frac{\partial z}{\partial y} + D \frac{\partial^2 z}{\partial x^2} + D \frac{\partial^2 z}{\partial y^2} - M_x(I_{ex} + F_x) - M_y(I_{ey} + F_y) - F_{x2} - F_{y2} \right\} \Delta t \quad (26)$$

A time waveform at the bed level was obtained by repeating this numerical integration during each ST measurement time.

The applicability of the HPDE obtained in the previous section was investigated by comparing the time waveform of the bed level. In this study, because the ST measurements were performed at 1-min intervals, Δt in the aforementioned calculation was set to 1 min. The method of calculating the riverbed variation amount used in the above comparison is a numerical calculation to obtain Δz after discretizing the Eq. (26) using the difference method.

Figure 8 shows the time waveform at the bed level. Figure 8 shows the time waveforms of (a) the left bank side, (b) central part, and (c) right bank side at 6.0 m from the upstream end. The red line shows the bed level of the measured value, and the blue line shows the bed level calculated from the formula.

Comparing the time waveform of the bed level by the calculation formula with the measured value showed that the time waveform of the bed level was well reproduced after 60 min of water flow in figures (a), (b), and (c).

As mentioned earlier, the time waveform was obtained by setting the time integration interval to 1 min. Although this time interval cannot be simply compared, it is much larger than the time interval in general numerical analysis. This result proved that the verification method that uses the aforementioned numerical integration and the applicability of the calculation formula that was derived in the previous section are excellent.

423

4.2.2 Riverbed Variation Amount

424

425

426

427

428

The verification in the previous section showed that the HPDE for Eq. (18) has sufficient applicability; however, its applicability decreased in the early stage of water flow. In this section, we discuss how much of this reduced applicability occupies the entire waterway and where it occurs. This is achieved using the riverbed variation amount. The riverbed variation was verified using the following equation.

$$\Delta z_* = |\Delta z_{obs} - \Delta z_{cal}|/d \times 100 \quad (27)$$

429

430

431

432

433

434

435

where Δz_{obs} is the riverbed variation obtained from the bed level between the two times that were measured by the ST. In addition, Δz_{cal} is the amount of riverbed variation by the HPDE and the calculation formula of the migrating speed. Δz_* in the aforementioned equation is a dimensionless quantity obtained by dividing the difference between the measured value of the riverbed variation amount and the calculated value using the equation based on the particle size. In addition, the difference between the two shows how much the divergence is based on particle size.

436

437

438

439

440

441

442

443

444

445

446

447

448

449

450

451

452

453

454

455

456

Figure 9 shows a plan view for the calculation accuracy of the riverbed variation Δz_* . Figure 9 shows the bed level, Δz_* from the top. (a) Considering the results for 1 min of water flow, Δz_* is generally within 100%, and the estimation accuracy of the waveform after 1 min at this time is the same as the particle size. From (a) 1 min of water flow to (h) 70 min, we can see that Δz_* is generally within 100% of the entire channel. When focusing on Δz_* from (b) 10 min to (f) 50 min of water flow, areas exceeding 500% occurred periodically in the longitudinal direction, and their total area accounted for approximately 40%. The bed surface at this time showed small irregularities that correspond to the periodically increasing and decreasing Δz_* . Δz_* is within 100% in all intervals because the small irregularities disappear after (g) 60 min. The results of (a) to (g) suggest that the accuracy of the estimation of the calculation formula for the migrating speed decreases when such small irregularities exist on the bed surface. However, the mathematical reason for this is currently unknown. The subject of this study is alternate bars, and it can be said that the authors' equation has sufficient applicability in the case in which alternate bars are dominant. The authors believe that the method used in this section for the numerical calculation of the riverbed variation amount and for the validation of the substitution of measured values into the discretized equation is appropriate. The reason for this is that if the method is essentially wrong, the riverbed variation amount estimated from the discretized HPDE and the measured values will not be consistent as shown in Figs. 8 and 9.

457

5 Quantification of the Migrating Speed for the Alternate Bars

458

459

460

461

462

The previous section confirmed that the HPDE and calculation formula for the migrating speed can reproduce the propagation phenomenon of alternate bars. In this section, the migrating speed of the alternate bars in each process during the occurrence and development is quantified using the calculation formula of the migrating speed.

463

464

5.1 Spatial Distribution of the Migrating Speed of the Alternate Bars

465

466

467

468

469

Figure 10 shows a plan view of the dimensionless migrating speed obtained by dividing the migrating speed obtained from the calculation formula for the bed level by the initial uniform flow velocity. The dimensionless migrating speed was used to understand the magnitude of the running water velocity and bed velocity. The above is based on the fact that the governing equations are often nondimensionalized with

470 uniform flow velocities during instability analysis (Callander, 1969; Kuroki & Kishi,
471 1984).

472 The figure shows the bed level and M/u_0 from the top. M is the magnitude
473 migrating speed, and u_0 is the uniform flow velocity. The area surrounded by the
474 hatch in the figure is the area in which the Shields number does not exceed the crit-
475 ical Shields number (hereinafter referred to as the effective Shields number); in this
476 area, the migrating speed is 0.

477 First, by focusing on (a) 1 min of water flow in the figure, M/u_0 has almost no
478 spatial distribution on a floor with an almost flat bed. We also confirmed that the
479 bed surface uniformly propagates at a speed of approximately 0.0015. After the bed
480 changes slightly from (b) 10 min to (e) 40 min, M/u_0 begins to show spatial distri-
481 bution. Subsequently, the spatial distribution of M/u_0 changes significantly from (g)
482 60 min of water flow to (l) 110 min. Considering this change with a spatial distribu-
483 tion from place to place, it can be seen that M/u_0 increases at the sedimentary part
484 and the front edge of the alternate bars, and it decreases at other locations.

485 Next, Fig. 11 illustrates a histogram that quantitatively shows the spatial dis-
486 tribution degree of M/u_0 at each time. The red and blue vertical lines in the figure
487 represent the mean \pm and standard deviation of M/u_0 at each time, and each value
488 is shown at the top of the figure. First, (a) the shape of the histogram after 1 min of
489 water flow is concentrated around an average value of 0.00143. In addition, because
490 the standard deviation is 0.00015, which is small with respect to the mean value,
491 it can be observed that the spatial distribution of M/u_0 at this time was small.
492 Then, from (b) 10 min of water flow to (g) 60 min of water flow when the alternate
493 bars occurred, the shape of the histogram became flat; the mean value of M/u_0 was
494 0.00126, and the standard deviation was 0.00023. Comparing (a) 1 min and (g) 60
495 min of water flow showed that although the mean value decreased by approximately
496 12 %, the standard deviation increased to nearly 1.5 times. This shows that the spa-
497 tial distribution of the migrating speed greatly expanded from the flat bed to the
498 occurrence of the alternate bars. After that, from (g) 60 min to (l) 110 min of water
499 flow, the flattening of the histogram, the increase in the standard deviation, and the
500 decrease in the mean value of M/u_0 became more significant. Comparing (a) 1 min
501 of water flow and (l) 110 min, which was the final time, showed that the mean value
502 of M/u_0 of (l) is 0.78 times from (a), and the standard deviation of (l) is 2.4 times
503 from (a).

504 These results demonstrated that the migrating speed of the alternate bars has
505 a spatial distribution, which expands from the stage of occurrence to the develop-
506 ment of the alternate bars.

507 5.2 Scale of the Migrating Speed of the Alternate Bars

508 This section discusses the scale of the migrating speed of the alternate bars. As
509 shown in the previous section, from Fig. 11, it can be confirmed that the migrating
510 speed has a spatial distribution, which gradually expands from 1 min of water flow
511 to 110 min. The non-dimensional migrating speed in the figure is divided by the uni-
512 form flow velocity on the flat floor. The scale of the migrating speed is in the order
513 of 10^{-4} to 10^{-3} of the uniform flow velocity at any location, regardless of the devel-
514 opmental state of the alternate bars. Therefore, it is inferred that the deformation
515 rate of the bed surface is sufficiently smaller than the deformation rate of running
516 water.

6 Applicability of the Formula for Calculating Migrating Speed in Actual Rivers

In section 4, we confirmed that the formula for calculating the migrating speed derived in this study has sufficient applicability in the flume experiment conducted in section 2, and in section 5, the spatial distribution of the migrating speed is quantified. In this section, we investigate the applicability of the formula to an actual river, where the scale, bed material, and hydraulic conditions are completely different from those in the flume experiment.

6.1 Flood Summary for Target River

The study river was the Chikuma River, which flows through Nagano Prefecture, Japan, as shown in Fig. 12(a). It is the longest river in Japan, with a channel length of 300 km. Owing to the outflow of water caused by Typhoon No. 19 in October 2019, the water level remained close to the bank level for approximately 10 h (Fig. 13(b)). This is the largest flow ever recorded and the eighth highest water level ever recorded in the history of observation.

Figure 1(a),(b) are aerial photographs of the river channel before and after the outflow in Ueda City shown in Fig. 12(b). The same figure shows that the alternate bars in the river channel were moved on a large scale by the outflow of water. The light blue line and the blue line in (b) of the same figure show the water route before and after the flood, respectively. Because the position of the water route depends on the position of the alternate bars, the distance moved by the water route at the time of outflow can be considered as the distance moved by the alternate bars before and after the flood, and it can be confirmed that the alternate bars traveled 450 to 800 m during this outflow.

6.2 Hydraulic Analysis for Calculation of Migrating Speed

To calculate the migrating speed obtained using our formula, one-dimensional unsteady flow calculations for a general cross section were performed to calculate the hydraulic quantities required for the calculations. The governing equations used in this calculation are the following two. The reason for the one-dimensional analysis is that it is difficult to obtain detailed information necessary for hydraulic calculations for actual rivers.

$$\frac{\partial A}{\partial t} + \frac{\partial Q}{\partial x} = 0 \quad (28)$$

$$\frac{\partial Q}{\partial t} + \frac{\partial}{\partial x} \left(\frac{Q^2}{A} \right) + gA \frac{\partial}{\partial x} (z + h) + \frac{gn^2 Q |Q|}{R^{4/3} A^2} = 0 \quad (29)$$

where A is the flow area, Q is the flow discharge, t is the time, x is the distance, z is the bed level, h is the water depth, n is Manning's roughness coefficient, and R is the hydraulic mean depth.

The target interval was from the 84-km point at Kuiseshita Observatory to the 109.5-km point at Ikuta Observatory, as shown in Fig. 12(b). For this calculation, we used transect survey data obtained at 500-m intervals and measured in 2017. Notably, from 2017, when the survey was conducted, to 2019, when the water was released, the river had not experienced any water outflow that would have significantly altered the channel geometry. The river bed material was given by varying it as a linear function in the computational section because it was 20 mm at the downstream end and 70 mm at the upstream end of the computational section. The roughness coefficient was given by the Manning–Strickler equation. The upstream

561 boundary condition is the flow discharge at Ikuta Observatory, shown in Fig. 13(a),
 562 and the downstream boundary condition is the water level at Kuisenshita Observa-
 563 tory, shown in Fig. 13(b).

564 Using the hydraulic quantities obtained from the above calculations, the mi-
 565 grating speed was calculated using the following equation. The same equation is
 566 a uni-dimensionalized expression obtained by finding the composite component of
 567 equations (19) and (20).

$$M = \frac{4(\tau_* - \tau_{*c})^{1/2} \sqrt{sgd^3} I_e}{sd(1 - \lambda)} \left[1 - \frac{\gamma'}{\tau_*^{1/2}} \left\{ 1 - \frac{1}{3\tau_*} (\tau_* - \tau_{*c}) \right\} \frac{\partial z}{\partial x} \right] \quad (30)$$

568 6.3 Estimation Result

569 Fig. 14 shows the longitudinal distribution of the estimated and measured
 570 migrating speed, and the same figure shows the interval of the calculation in Fig.
 571 1. The green line in the figure shows the calculation results at each flow discharge
 572 marked in Fig. 13, from 1000 m³/s, when sediment began moving throughout the
 573 section, to the peak flow discharge. The migrating speed was calculated using the
 574 uni-dimensionalized migrating speed equation shown in equation (30), using the hy-
 575 draulic mean depth, energy slope, and Shields number. The gray marks in the fig-
 576 ure indicate the measured migrating speed. The average migrating speed during the
 577 flood period was calculated based on the relationship between the travel distance of
 578 the water route and the travel time, which was assumed to be approximately 29 h of
 579 active sediment transport based on the flow hydrograph and analysis results.

580 Focusing on the calculation results of the migrating speed at each flow dis-
 581 charge, we can see that the migrating speed has a spatial distribution at all flow dis-
 582 charge, and it increases as the flow discharge increases.

583 A comparison of the calculated and measured migrating speeds confirms that
 584 the calculated values are about half of the measured values, but they are generally
 585 consistent with the measured values, and the waveforms are also generally consis-
 586 tent, except for those at the 104-km point. These results suggest that the hydraulic
 587 quantity in the downstream direction is dominant in defining the migrating speed.

588 7 Discussion

589 In this section, we discuss the following four subsections of the migrating speed
 590 of alternate bars.

591 7.1 Main Dominant Physical Quantity of Movement Speed

592 In this study, the migrating speed of alternate bars is quantified by both mea-
 593 surements and estimations. The validity of the calculated migrating speed is also
 594 confirmed. In this section, we discuss the mathematical structure of the equation to
 595 understand the main dominant physical quantity of the migrating speed.

596 Fig. 15 shows three relationships between the energy slope, the Shields num-
 597 ber, and the dimensionless migrating speed at the final time of the flume experi-
 598 ment. The same figure indicates that the dimensionless migrating speed is propor-
 599 tional to the Shields number and energy slope. Because the dimensionless migrating
 600 speed is a product of Shields number and energy slope, it is difficult to say which is
 601 dominant. However, in this experiment, the energy slope is closer to the order of the
 602 dimensionless migrating speed, indicating that the energy slope is the more domi-
 603 nant physical quantity.

7.2 Approximate Description of Migrating Speed

In the previous section, we suggested that the energy slope is the dominant physical quantity that determines the order of migrating speed. From this, it can be inferred that the energy slope can be used to describe the approximate migrating speed. Whether this approximate description is possible was examined based on the relationship between M/u_0 and $0.4 \times I_e$ in Fig. 16. The correlation coefficients between the two at each time are shown in the figure. The value of 0.4 multiplied by the same equation is a coefficient determined from the particle size, which is one of the variables in the denominator of equations (19) and (20).

Considering the relationship between M/u_0 and $0.4 \times I_e$, we can see that the relationship is almost one-to-one at all times. The correlation coefficients are above 0.9 on average, indicating that the two have a strong positive correlation. These results suggest that an approximate description of the migrating speed of alternate bars using energy slope is possible.

7.3 Decreasing Factor for the Migrating Speed of the Alternate Bars

This subsection discusses the decreasing factor for migrating speed of the alternate bars. Figure 17 shows the average longitudinal distributions of the (a) migrating speed, (b) energy line, hydraulic grade line, and bed line over time. The sediment condition for the flume experiment in this study is that no sediment supply exists. Therefore, the bed level and each hydraulic head decreased with time in the upstream section of the moving bed. The water level and energy head in the same section also decreased from the initial stage, and the water surface slope and energy slope, including the riverbed slope, became more moderate. In contrast, the water depth did not change much from the initial value in the whole section. In addition, it can be seen that (a) the migrating speed in the same section decreased from the initial value. Next, if we focus on the point 5.5 m from the upstream end, we can see that the water depth has hardly changed since the initial value, the energy slope has increased, and the migrating speed has also increased.

As shown in Eq. (19) and Eq. (20), there are three dominant physical quantities of the migrating speed, which are grain size, non-dimensional scavenging force, and energy gradient, except for the component decomposition part. The dominant physical quantities of the Shields number are grain size, water depth, and energy slope. Therefore, we can say that there are three physical quantities that effectively govern the migrating speed, which are grain size, water depth, and energy slope. Focusing on these dominant physical quantities, the decreasing factors of the migrating speed of alternate bars in this experiment can be summarized as follows. First, because the particle size in this experiment is a single particle size, it is assumed that there is no change in the migrating speed due to changes in the particle size. Because the water depth also slightly changed on average, it can be inferred that there was little change in the migrating speed due to changes in the water depth. In contrast, the energy slope was significantly reduced, and the migrating speed was considerably decreased along with it. This decrease in the energy slope is due to the decrease in the bed level caused by the no sediment supply at the upstream end. These results indicate that the reason for the decrease in the migrating speed of the alternate bars in this experiment is the decrease in the energy slope due to the decrease in the bed slope.

Eekhout et al. (2013) observed the occurrence and development processes of alternate bars in an actual river and reported that the bed slope decreased when the migrating speed of alternate bars was decreased. The migrating speed of the alternate bars decreased owing to changes in grain size or water depth because their study had the same target section and the same flood magnitude during the observa-

655 tion period. Based on the results of this experiment, we assumed that the migrating
 656 speed decreased owing to the reduction in the energy slope caused by a decrease in
 657 the bed slope.

658 **7.4 Comparison of the Migrating Speed of our Method with that of** 659 **Instability Analysis**

660 The conditions for the occurrence and non-occurrence of alternate bars have
 661 been determined by instability analysis for small perturbations given as initial con-
 662 ditions (Callander, 1969; Kuroki & Kishi, 1984). In these instability analyses, the
 663 migrating speed of small perturbations was calculated. Although the form of the
 664 equation and the process of deriving the equation are different, it can be inferred
 665 that the equation for migrating speed based on instability analysis and the equation
 666 for migrating speed in this study were essentially the same. In this section, we com-
 667 pare the migrating speed of our method with that of instability analysis.

668 Fig. 18 shows the relationship between the migrating speed of our method and
 669 the migrating speed of instability analysis. The vertical axis of the figure is the mi-
 670 grating speed of our method, which is shown as a box-and-whisker diagram for three
 671 time periods: 1 min at the initial river bed, 50 min at the time of sandbar occur-
 672 rence, and 120 min at the final time under each hydraulic condition shown in Table
 673 1. The horizontal axis of the figure is the migrating speed for the instability analysis
 674 and shows the results of each of the linear and weakly nonlinear analyses obtained
 675 when the same hydraulic conditions were given as in Table 1. The migrating speed
 676 for instability analysis was calculated from the equation proposed by Bertagni and
 677 Camporeale (2018), shown below.

$$678 \quad M_{*(L.)} = -\frac{\text{Im}[\Omega]}{k} \quad (31)$$

$$M_{*(W.N.L.)} = -\left(\frac{\text{Im}[\Omega] - \text{Im}[\Xi] \frac{\text{Im}[\Omega]}{\text{Re}[\Xi]}}{k}\right) \quad (32)$$

679 where $M_{*(L.)}$ is the non-dimensional migrating speed from linear instability analysis,
 680 $M_{*(W.N.L.)}$ is the non-dimensional migrating speed from weakly nonlinear instability
 681 analysis, Ω is the amplification factor, k is the wavenumber, and Ξ is the Landau
 682 Coefficient. For details on how to calculate the amplification factor Ω and Landau
 683 Coefficient Ξ , please refer to the original publication (Bertagni & Camporeale, 2018).

684 (a) to (c) in the same figure show the migrating speed of each bars from the
 685 occurrence to the development stage. First, the vertical axis of (a) to (c) in the same
 686 figure shows that the migration speed of the authors decreased on average from the
 687 occurrence to the development of the alternate bars. Next, focusing on the migration
 688 speed of the instability analysis, the migrating speed of the weakly nonlinear insta-
 689 bility analysis is slower than that of the linear instability analysis. The migrating
 690 speed of the linear instability analysis is those of the dominant wave number at the
 691 time of alternate bars occurrence, while the migrating speed of the weakly nonlinear
 692 instability analysis is those of the dominant wave number at the time of alternate
 693 bars development. Thus, the trend of the migrating speed of the alternate bars from
 694 the occurrence to the development is consistent between the author's method and
 695 the instability analysis.

696 In the previous section and in Fig. 11, we have shown that the migrating speed
 697 of alternate bars has a spatial distribution and that it varies with time. Neverthe-
 698 less, the migrating speeds is generally the same regardless of the time of occurrence
 699 and the stage of development. The reason for this is that, as can be seen immedi-

ately from Fig. 11, the scale of the change in the spatial distribution of the migrating speed during the development stage of the alternate bars is not much different from that during the occurrence of the alternate bars, and the statistical variance is as small as 10^{-3} .

8 Conclusion

In this study, we first conducted flume experiments under the condition that alternate bars can occur and develop. We measured the hydraulic quantity and bed shape using a high spatial resolution. Next, we quantified the migrating speed of the alternate bars using the measured values obtained in the flume experiments and the calculation formula. This study determined that the migrating speed of the alternate bars has a spatial distribution, and it changes with time. The results of this study are presented below.

- 1) We measured the water level and bed level of the occurrence and development process of alternate bars and demonstrated that the migrating speed of the alternate bars has a spatial distribution from the measured geometric shape of the bed surface.
- 2) The HPDE for bed level z and the formula for the migrating speed were derived to quantitatively determine the migrating speed of the alternate bars. By comparing the measured values with the flume experiments, we demonstrated that the formula can appropriately describe the propagation phenomenon of the alternate bars.
- 3) By calculating the migrating speed of the alternate bars based on the aforementioned formula, we clarified that the migrating speed of the alternate bars has a spatial distribution. In addition, the spatial distribution changes with the development of bars over time, which was unconfirmed in the literature.
- 4) We observed that the migrating speed of the alternate bars is about three to four orders of magnitude smaller than the initial uniform flow velocity, regardless of the developmental state and the location of the bars.
- 5) Our method is generally applicable to actual rivers, where the scale and hydraulic conditions are different from those in the flume experiments.
- 6) It is suggested that the reason for the decrease in the migrating speed of the alternate bars is the decrease in the energy slope due to the decrease in the bed slope.
- 7) we showed that the spatial distribution of migrating speed expands during the occurrence and development of alternate bars, based on the measured data and the estimated equation of migrating speed derived by the authors, respectively. However, the scale of the statistical variance of its spatial distribution was not large enough to be of different orders of magnitude.
- 8) The results of the comparison between the migrating speeds of the instability analysis and of the author's method showed that the two are in general agreement during the occurrence and development of the alternate bars. As the scale of the statistical variance of the spatial distribution of the migrating speed is not large, the instability analysis can provide the average migrating speed of the bar.

Acknowledgments

The data used in this study can be accessed at (Ishihara & Yasuda, 2022). For details of the data, please refer to the enclosed README.md. This work was supported by JSPS KAKENHI Grant Numbers JP21H04596, JP20K20543, and JICE(No.19005 and No. 20004), Japan Institute of Country-ology and Engineering. The contents of

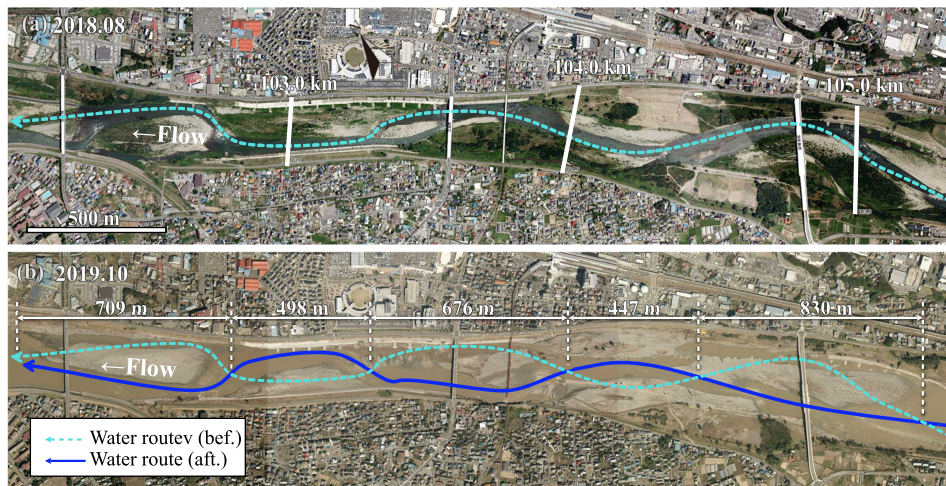


Figure 1. Aerial photos of the Chikuma river of Japan (a) before the flood, (b) after the flood (「Part 2 Chikumagawa teibou chousa iinnkai shiryō」 (Ministry of Land, Infrastructure, Transport and Tourism) (<https://www.hrr.mlit.go.jp/river/chikumagawateibouchousa/chikuma-02.pdf>) created by processing).

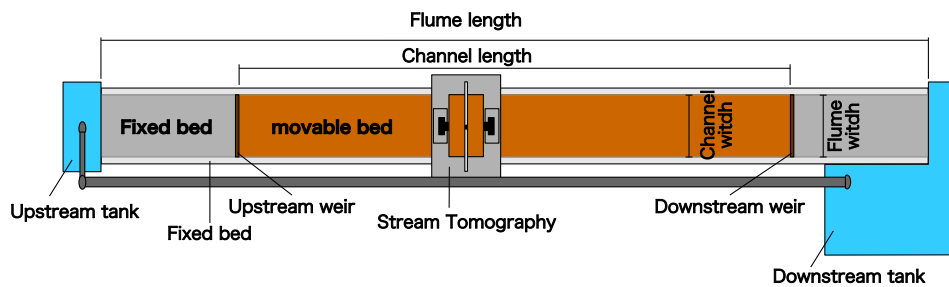


Figure 2. Plan view of the experimental flume.

749 this paper have been greatly improved by the comments of the reviewers. I also used
 750 the Mathematica code provided in Supporting Information in Bertagni et al.'s paper
 751 (Bertagni & Camporeale, 2018), with input from reviewer Bertagni, to improve the
 752 content. The essential remarks made by associate editor and the reviewers helped
 753 us to refine our research significantly. I would like to express my gratitude to asso-
 754 ciate editor and the reviewers. We would like to thank Editage (www.editage.com)
 755 for English language editing.

756 References

- 757 Adami, L., Bertoldi, W., & Zolezzi, G. (2016). Multidecadal dynamics of alternate
 758 bars in the alpine rhine river. *Water Resources Research*, *52*(11), 8938-8955.
 759 doi: <https://doi.org/10.1002/2015WR018228>
 760 Bertagni, M. B., & Camporeale, C. (2018). Finite amplitude of free alternate bars
 761 with suspended load. *Water Resources Research*, *54*(12), 9759-9773. doi:
 762 <https://doi.org/10.1029/2018WR022819>
 763 Callander, R. A. (1969). Instability and river channels. *Journal of Fluid Mechanics*,
 764 *36*(3), 465-480. doi: 10.1017/S0022112069001765
 765 Colombini, M., Seminara, G., & Tubino, M. (1987). Finite-amplitude alternate bars.
 766 *Journal of Fluid Mechanics*, *181*, 213-232. doi: 10.1017/S0022112087002064

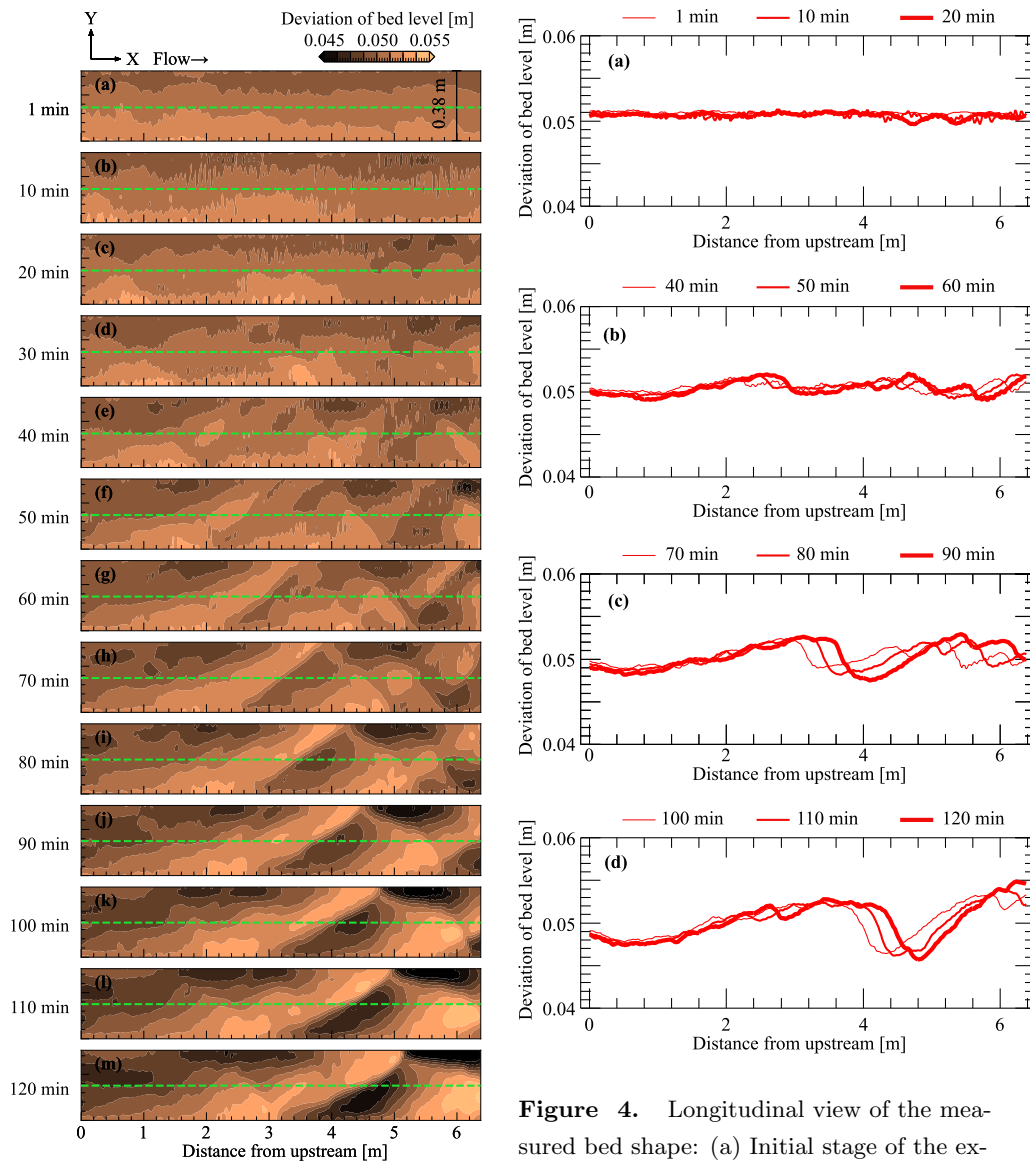


Figure 3. Temporal changes of the plan view in the observed bed topography.

Figure 4. Longitudinal view of the measured bed shape: (a) Initial stage of the experiment, (b) occurrence of alternate bars, (c) intermediate stage of the experiment, and (d) final stage of the experiment.

- 767 Colombini, M., & Tubino, M. (1991). Finite-amplitude free bars: A fully nonlinear
 768 spectral solution. *in Sand Transport in Rivers, Estuaries and the Sea*, edited by
 769 R. Soulsby and R. Bettes, A. A. Balkema, Brookfield, Vt., 163-169.
- 770 Crosato, A., Desta, F. B., Cornelisse, J., Schuurman, F., & Uijttewaal, W. S. J.
 771 (2012). Experimental and numerical findings on the long-term evolution of mi-
 772 grating alternate bars in alluvial channels. *Water Resources Research*, *48*(6).
 773 doi: 10.1029/2011WR011320
- 774 Crosato, A., Mosselman, E., Beidmariam Desta, F., & Uijttewaal, W. S. J. (2011).
 775 Experimental and numerical evidence for intrinsic nonmigrating bars in allu-
 776 vial channels. *Water Resources Research*, *47*(3). doi: 10.1029/2010WR009714
- 777 Eekhout, J. P. C., Hoitink, A. J. F., & Mosselman, E. (2013). Field experiment
 778 on alternate bar development in a straight sand-bed stream. *Water Resources*
 779 *Research*, *49*(12), 8357-8369. doi: 10.1002/2013WR014259

- 780 Federici, B., & Seminara, G. (2003). On the convective nature of bar instability.
781 *Journal of Fluid Mechanics*, 487, 125-145. doi: 10.1017/S0022112003004737
- 782 Fujita, Y., Koike, T., Furukawa, R., & Muramoto, Y. (1985). Experiments on the
783 initial stage of alternate bar formation. *Disaster Prevention Research Institute*
784 *Annals (in Japanese)*, 28(B-2), 379-398.
- 785 Fujita, Y., & Muramoto, Y. (1982). Experimental study on stream channel processes
786 in alluvial rivers. *Bulletin of the Disaster Prevention Research Institute*, 32(1),
787 49-96.
- 788 Fujita, Y., & Muramoto, Y. (1985). Studies on the process of development of al-
789 ternate bars. *Bulletin of the Disaster Prevention Research Institute*, 30(3),
790 55-86.
- 791 Hayashi, T., Ozaki, Y., & Onishi, K. (1982). On the mechanism of occurrence of
792 three-dimensional bed configurations. *PROCEEDINGS OF THE JAPANESE*
793 *CONFERENCE ON HYDRAULICS (in japanese)*, 26, 17-24. doi: 10.2208/
794 prohe1975.26.17
- 795 Hoshino, T., Yasuda, H., & Kurahashi, M. (2018). Direct measurement method
796 of formation processes of alternate bars. *J. Jpn. Soc. Civ. Eng. Ser. Applied*
797 *Mechanics.(in Japanese)*, A2. 74(1), 63-74.
- 798 Ikeda, H. (1983). Experiments on bedload transport, bed forms, and sedimentary
799 structures using fine gravel in the 4-meter-wide flume..
- 800 Ishihara, M., & Yasuda, H. (2022). *Dataset*. (<https://doi.org/10.4121/16788778.v1>)
- 801 Iwagaki, Y. (1956). Hydrodynamical study on critical tractive force. *Transactions*
802 *of the Japan Society of Civil Engineers (in Japanese)*, 1956(41), 1-21. doi:
803 10.2208/jscej1949.1956.41_1
- 804 Izumi, N., & Pornprommin, A. (2002). Weakly nonlinear analysis of bars with
805 the use of the amplitude expansion method. *Doboku Gakkai Ronbunshu*,
806 2002(712), 73-86. doi: 10.2208/jscej.2002.712_73
- 807 Kennedy, J. F. (1963). The mechanics of dunes and antidunes in erodible-
808 bed channels. *Journal of Fluid Mechanics*, 16(4), 521-544. doi: 10.1017/
809 S0022112063000975
- 810 Kinoshita, R. (1958). Experiment on dune length in straight channel. *Journal of*
811 *the Japan Society of Erosion Control Engineering (in japanese)*, 1958(30), 1-8.
812 doi: 10.11475/sabo1948.1958.30_1
- 813 Kinoshita, R. (1961). Investigation of channel deformation in ishikari river. *Rep.*
814 *Bureau of Resources, Dept. Science & Technology, Japan. (in japanese)*.
- 815 Kuroki, M., & Kishi, T. (1984). Regime criteria on bars and braids in allu-
816 vial straight channels. *Proceedings of the Japan Society of Civil Engineers*,
817 1984(342), 87-96. doi: 10.2208/jscej1969.1984.342_87
- 818 Lanzoni, S. (2000a). Experiments on bar formation in a straight flume: 1. uni-
819 form sediment. *Water Resources Research*, 36(11), 3337-3349. doi: 10.1029/
820 2000WR900160
- 821 Lanzoni, S. (2000b). Experiments on bar formation in a straight flume: 2. graded
822 sediment. *Water Resources Research*, 36(11), 3351-3363. doi: 10.1029/
823 2000WR900161
- 824 Miwa, H., Daido, A., & Katayama, T. (2007). Effects of water and sediment dis-
825 charge conditions on variation in alternate bar morphology. *Proceedings of hy-*
826 *draulic engineering (in japanese)*, 51, 1051-1056. doi: 10.2208/prohe.51.1051
- 827 Nagata, N., Muramoto, Y., Uchikura, Y., Hosoda, T., Yabe, M., Takada, Y., &
828 Iwata, M. (1999). On the behaviour of alternate bars under several kinds of
829 channel conditions. *PROCEEDINGS OF HYDRAULIC ENGINEERING (in*
830 *japanese)*, 43, 743-748.
- 831 Nelson, P., & Morgan, J. (2018, 09). Flume experiments on flow and sediment
832 supply controls on gravel bedform dynamics. *Geomorphology*, 323. doi:
833 10.1016/j.geomorph.2018.09.011
- 834 Ozaki, S., & Hayashi, T. (1983). On the formation of alternating bars and braids

- 835 and the dominant meander length. *Proceedings of the Japan Society of Civil*
 836 *Engineers*, 1983(333), 109-118. doi: 10.2208/jscej1969.1983.333_109
- 837 Podolak, C. J. P., & Wilcock, P. R. (2013). Experimental study of the response of
 838 a gravel streambed to increased sediment supply. *Earth Surface Processes and*
 839 *Landforms*, 38(14), 1748-1764. doi: 10.1002/esp.3468
- 840 Schielen, R., Doelman, A., & Swart, H. E. (1993). On the nonlinear dynamics of free
 841 bars in straight channels. *Journal of Fluid Mechanics*, 252, 325-356.
- 842 Seminara, G. (2010). Fluvial sedimentary patterns. *Annual Review of Fluid Mechan-*
 843 *ics*, 42(1), 43-66. doi: 10.1146/annurev-fluid-121108-145612
- 844 Shimizu, Y., & Itakura, T. (1989). Calculation of bed variation in alluvial channels.
 845 *Journal of Hydraulic Engineering*, 115(3), 367-384. doi: 10.1061/(ASCE)0733
 846 -9429(1989)115:3(367)
- 847 Tubino, M. (1991). Growth of alternate bars in unsteady flow. *Water Resources*
 848 *Research*, 27(1), 37-52. doi: 10.1029/90WR01699
- 849 Venditti, J. G., Nelson, P. A., Minear, J. T., Wooster, J., & Dietrich, W. E. (2012).
 850 Alternate bar response to sediment supply termination. *Journal of Geophysical*
 851 *Research: Earth Surface*, 117(F2). doi: 10.1029/2011JF002254
- 852 Watanabe, A., Fukuoka, S., Yasutake, Y., & Kawaguchi, H. (2001). Groin arrange-
 853 ments made of natural willows for reducing bed deformation in a curved chan-
 854 nel. *Advances in river engineering (in japanese)*, 7, 285-290.
- 855 Zhang, Z. (1998). Flexible new technique for camera calibration. *Technical Report*
 856 *MSR-TR-98-71, Microsoft Research, Microsoft Corporation.*

857 **Appendix A Stream Tomography**

858 Here, we describe the measurement principle of the stream tomography used in
 859 the flume experiment.

860 **A1 Outline of the Measurement Device and Measurement Procedure**

862 Figure A1 show the overall plan view of the measurement device and the lay-
 863 out of the equipment. The overall configuration of the measurement device includes
 864 a laser sheet light source and a traveling platform that has two digital cameras in-
 865 stalled. The laser sheet light source used in this study is a yttrium aluminum garnet
 866 (YAG) laser with a wavelength of 532 nm. In addition, to promote the emission of
 867 the laser light in water, the water used in the flume experiment was green because
 868 of dissolved sodium fluorescein. As shown in Fig. A1 the two digital cameras sand-
 869 wiched the laser sheet light source so it was upstream and downstream on the trav-
 870 eling platform. The camera was installed such that it was diagonally downward to-
 871 ward the center of the stream. The three-dimensional coordinates of the water level
 872 and bed level by the ST can be obtained based on the intersection of the origin coor-
 873 dinates (lens center point) for each of the two aforementioned cameras and the geo-
 874 metric vector that connects the water level and bed position that will be measured.

875 **A2 Physical principles**

876 This measurement method is based on the principle of triangulation, in which
 877 three-dimensional coordinates are obtained from the intersection of two geometric
 878 vectors connecting two known points and a measurement target. In this study, the
 879 vectors of the directed line segments are referred to as geometric vectors. The geo-
 880 metric relationship in this method is shown in Fig. A2. The water surface level can
 881 be calculated as the intersection h of two geometric vectors connecting the origin
 882 coordinates of each of the two cameras and the laser reflection coordinates of the
 883 water surface, and the water bottom level is calculated as the intersection b of two

884 geometric vectors connecting the water surface level and the laser reflection coord-
 885 inates of the water bottom level. Of these, the calculation of the 3-D coordinates
 886 of the water bottom level requires consideration of refraction at the water surface.
 887 In this method, the refraction of the reflected laser beam at the bottom of the wa-
 888 ter surface is corrected based on Snell’s law, and the 3-D coordinates of the bottom
 889 level are obtained based on the water surface level that can be obtained areally. The
 890 measurement procedure comprises the following four steps: 1) video recording with
 891 two cameras while the carriage is moving in the downstream direction, 2) analysis
 892 of the intersection points between the laser sheet and the water/bed surface in the
 893 videos, 3) calculation of the water surface level h based on triangulation, and 4) cal-
 894 culation of the bed level b by correction based on Snell’s law. The internal and ex-
 895 ternal parameters of the camera required as the origin of the calculation were cal-
 896 culated using Zhang’s calibration method (Zhang, 1998). The origin coordinates
 897 of the two cameras were calculated for upstream C_u and downstream C_d , respec-
 898 tively. C_u and C_d are number vectors with 3-D spatial coordinates as components,
 899 $C_u = (x_{c_u}, y_{c_u}, z_{c_u})$ and $C_d = (x_{c_d}, y_{c_d}, z_{c_d})$.

900 A3 Image analysis

901 To measure the geometries of the water surface and the water bottom, pixel
 902 numbers corresponding to the water surface and bed surface were detected in the
 903 captured images. i and j represent the pixel numbers in the horizontal and vertical
 904 directions of the image, respectively. The pixel number corresponding to the inter-
 905 section of the laser sheet and the water surface was detected using Canny, a function
 906 of OpenCV(<https://opencv.org>), and by specifying the green lightness range as the
 907 threshold. Similarly, the pixel number corresponding to the intersection of the laser
 908 sheet and the bed surface was detected as the maximum value of the green lightness
 909 in the j -direction. The reflectance intensity of the green luminosity at the water sur-
 910 face and bottom varies depending on the experimental environment, the intensity of
 911 the laser beam, and the riverbed material. In particular, the detection threshold of
 912 the water surface must be adjusted according to the measurement conditions. In this
 913 study, the water surface detection threshold was set to a range in which the green
 914 luminosity exceeded 40 but did not exceed 160.

915 A4 Obtaining the water surface gradient for refraction correction

916 This subsection presents a procedure for calculating the water surface gradi-
 917 ent required for the calculation of the bed level by refraction correction based on
 918 Snell’s law, using a grid of water surface measurements. Numerous water surface
 919 measurements can be conducted in the longitudinal and transverse directions with
 920 the spatial resolution described above. Because a gradient of the water surface is
 921 required for refraction correction of the bed surface measurement, a structured dis-
 922 crete function $H_{(i,j)}$ is created by arranging h in Fig. A2 in a grid of arbitrary in-
 923 tervals (Fig. A3). The bed level b was calculated from the geometric relationship
 924 shown in Fig. A4. Accurate refraction correction requires C_{hu} and C_{hd} , as shown
 925 in Fig. A4, and the water surface slope (normal vector of the water surface) n_u and
 926 n_d at that point. $C_{hu}(C_{hd})$ is the intersection vector between, the vector connect-
 927 ing $C_u(C_d)$ and the identified pixel at the bottom, and the water surface. Because
 928 $n_u(n_d)$ represents the water surface gradient at $C_{hu}(C_{hd})$, it can be calculated using
 929 $H_{(i,j)}$. The refractive indices used for refraction correction were air ($n_{air} = 1.0$) and
 930 water ($n_{water} = 1.333$), respectively.

931

A5 Validation

932

933

934

935

936

937

938

939

940

941

942

943

944

945

946

947

948

949

950

951

The following experiments were conducted to verify the accuracy and applicability of ST. Experiments 1 to 3 were conducted without sand, using objects of known shapes (Fig. A5), and Experiment 4 was conducted in a flow over a sand wave of the scale often observed in experiments on sandbars. To verify the accuracy of measurement, the plane of the rectangular top surface placed on the bottom was used, as shown in Fig. A5, because the true value shape of the flume bottom was unknown. The measurement principle of ST is such that the measurement error becomes large when the geometric shape of the bottom surface abruptly changes in the longitudinal direction, and a blind spot exists in the view of the camera. Therefore, hemispheres were used for verification to confirm the follow-up of the measurements in the longitudinal direction. The hemisphere has an infinite divergence of bed slope at the point of contact with the bottom. The size of the hemisphere was $r = 2.5$ cm, which is larger than the maximum wave height of the sand waves ($=2$ cm), as confirmed in the preliminary experiments. The flow depth in experiments 1 to 3 was set to be 1.5 to 4 cm in the measurement range, which is a condition for the hemisphere to be underwater. The flow depth in the experiments on sand bars in this flume was approximately 1 to 3 cm. In Experiment 4, the bottom of the channel was covered with 5 cm of silica sand ($D_{50} = 0.755$ mm), which is commonly used in moving-bed experiments, and the discharge was 2.5 l/sec for 2 h to confirm the formation of sandbars. Subsequently, the sandbar was drained and fixed with cement.

952

A6 Experiment 1 (dry)

953

954

The purpose of Experiment 1 was to verify the validity of the triangulation-based ST and its angular tracking capability.

955

956

957

958

959

960

961

962

963

964

965

966

In the upper part of Fig. A6, the plane of the rectangle was measured five times, and the measurement results are shown in three measurement lines for the longitudinal and transverse directions. The lines were set at 3 cm intervals for both longitudinal and transverse measurements. The upper solid line in Fig. A6 is an estimate obtained from the least-squares method of the measurement results and is regarded as the true value in the evaluation of this section. The true value lines are skewed in both longitudinal and transverse sections, but this is due to the skewness of the measuring device or the water channel and is unrelated to the measurement accuracy. The measurement error of the triangulation is shown by the difference from the true value in the lower part of Fig. A6. The error of the measurement was less than 0.03 cm at all measurement points in each longitudinal and transverse direction.

967

968

969

970

971

972

973

974

975

976

977

To verify the angular-tracking properties, Fig. A7 shows the measurement results of three hemispheres lined up in the longitudinal direction and the solid line of the true value superimposed. The measurement results are shown by superimposing the results of five measurements in three hemispheres (15 measurements in total). The vertical error of each measurement is shown on the right side of Fig. A7. While the error was less than 0.1 cm near the hemisphere apex, the accuracy deteriorated as the angle to the bottom increased or decreased. Using an error of 0.2 cm as a threshold, the following angle was calculated to be approximately 60° , which is consistent with the camera's overhead angle. The accuracy is lower for hemispheres than for rectangles because the timing of the camera shots cannot be perfectly matched.

978 **A7 Experiment 2 (Still water)**

979 Experiment 2 was conducted to verify the validity of the ST water surface
980 measurements and bottom measurements with refraction correction.

981 In the upper part of Figs. A8,A9, the measurement results of the hydrostatic
982 surfaces of three measurement lines in the longitudinal and transverse directions and
983 the estimated values obtained by the least-squares method as true values as in A6
984 are shown as solid lines. The position of the measurement line in the transverse di-
985 rection was $x = 100, 200, 300$ cm with $x = 0$ cm as the starting point. The position
986 of the measurement line in the longitudinal direction was $y = 7.5, 22.5, 37.5$ cm with
987 $y = 0$ cm on the right bank of the channel. The error from the true value is shown
988 in the lower part of Figs. A8,A9. The measurement results include a characteristic
989 error which seems to be affected by the movement of the carriage, but the cause re-
990 mains unknown. The magnitude of the error varies depending on the location, but
991 it is less than 0.05 cm for most of the longitudinal transects and about 0.1 cm at the
992 maximum.

993 Fig. A10 shows the measurement results of the hemisphere in still water and
994 the solid line of the true value, as in Subsection A6, overlaid with results of 15 mea-
995 surements. The measurement of the bottom surface in still water requires refrac-
996 tion correction based on the measured values at the water surface, but there was no
997 degradation in accuracy. In addition, the angular follow-up was approximately the
998 same.

999 **A8 Experiment 3 (Flowing water)**

1000 Experiment 3 was conducted to verify the validity of the measurements under
1001 flowing water conditions. Fig. A11 shows the measurement results of the hemisphere
1002 at the bottom of the flowing water condition and the solid line of the true value, su-
1003 perimposed with the results of 15 measurements as in Subsection A6. The measure-
1004 ment accuracy and angular follow-up remained almost unchanged from those in the
1005 dry and still water conditions.

1006 **Appendix B Validity of the Pseudo-steady Flow Assumption Ap-**
1007 **plied to Bars-Scale Riverbed Waves**

1008 This section describes the validity of the pseudo-steady flow assumption ap-
1009 plied to the bar-scale riverbed waves. In this study, we introduced the assumption
1010 of a pseudo-steady flow when deriving the HPDE for bed level z . This assumption
1011 is often introduced in stability analyses of bar-scale riverbed waves (Callander, 1969;
1012 Kuroki & Kishi, 1984). In the aforementioned stability analysis, we assumed that
1013 the migrating speed of the bed is sufficiently slower than the propagation velocity
1014 of the flow, and the flow can be treated as a pseudo-steady flow if the flow rate is
1015 constant. Based on this assumption, for stability analysis, we ignore the term of the
1016 time gradient in the continuity equation of flow and the equation of motion of flow
1017 among the governing equations that are used in the analysis. The aforementioned
1018 assumptions are considered to be valid. This is because the stability analysis ex-
1019 plains the occurrence and developmental mechanisms of alternate bars. However,
1020 to the best of our knowledge, whether the term of the time gradient of the flow can
1021 actually be ignored cannot be confirmed from the actual phenomenon. Therefore, we
1022 verified whether the term of the flow time gradient can be ignored with ST measure-
1023 ment values and hydraulic analysis.

1024 The aforementioned verification was performed by comparing the contributions
1025 of each term in the equation of motion for flow.

$$\frac{1}{g} \frac{\partial u}{\partial t} + \frac{u}{g} \frac{\partial u}{\partial x} + \frac{\partial H}{\partial x} + I_{ex} = 0 \quad (\text{B1})$$

1026 where H is the water level. As the explanation of the various physical quantities
1027 has already been provided, it is omitted here. The contribution of each term in the
1028 aforementioned equation was calculated for each ST measurement time, and the
1029 magnitudes were compared.

1030 $\partial H/\partial x$ was obtained with the measured value of the water level of the ST.
1031 Other terms were obtained with the results of the hydraulic analysis, which is de-
1032 scribed in Section 4.1 in the main text. The time interval and spatial interval of the
1033 calculation were 1 min and 2 cm, respectively, which are the time resolutions and
1034 spatial resolutions of ST. The flow velocity and migrating speed of the y component
1035 under the experimental conditions were 10^{-4} to 10^1 of the x components at any lo-
1036 cation regardless of the developmental state of the alternate bars. For simplicity, the
1037 y component is ignored in this section.

1038 Figure B1 shows the time change of the box-beard diagram that displays the
1039 contribution of each term. This figure shows the (a) local term, (b) advection term,
1040 (c) pressure term, and (d) friction term, which correspond to the order of each term
1041 in Eq. (B1). The figure shows that although the (b) advection term, (c) pressure
1042 term, and (d) friction term dominate the flow at any time, it can be confirmed that
1043 (a) the local term can be ignored because it is smaller than the aforementioned three
1044 terms. Even if the advection term with the smallest contribution in (b), (c), and (d)
1045 is compared with the local term, the contribution of the local term is 10^{-4} to 10^{-2}
1046 of the (b) advection term. In addition, it can be observed that the local term is ex-
1047 tremely small. From this, it is inferred that it is physically appropriate to ignore the
1048 time gradient of flow in the alternate bars.

1049 Appendix C Derivation of the Two-Dimensional Equation of the 1050 Water Surface Profile

1051 Appendix C presents the derivation processes of the two-dimensional equation
1052 of the water surface profile to derive the HPDE for the bed level. The governing
1053 equations used for the derivation consist of the following continuous equations and
1054 the equations of motion. When deriving the equation, the flow can be treated as a
1055 pseudo-steady-state flow based on the verification results in Appendix B. Therefore,
1056 the following continuous equations and equations of motion were used for the deriva-
1057 tion.

$$\frac{\partial[hu]}{\partial x} + \frac{\partial[hv]}{\partial y} = 0 \quad (\text{C1})$$

1058

$$\frac{u}{g} \frac{\partial u}{\partial x} + \frac{v}{g} \frac{\partial u}{\partial y} + \frac{\partial z}{\partial x} + \frac{\partial h}{\partial x} + I_{ex} = 0 \quad (\text{C2})$$

1059

$$\frac{u}{g} \frac{\partial v}{\partial x} + \frac{v}{g} \frac{\partial v}{\partial y} + \frac{\partial z}{\partial y} + \frac{\partial h}{\partial y} + I_{ey} = 0 \quad (\text{C3})$$

1060 As an explanation of the various physical quantities has already been provided, it is
1061 omitted here.

1062 The derivation of $\partial h/\partial x$ is described as follows. First, applying the product
1063 rule to Eq. (C1) results in the following equation.

$$h \frac{\partial u}{\partial x} + u \frac{\partial h}{\partial x} + h \frac{\partial v}{\partial y} + v \frac{\partial h}{\partial y} = 0 \quad (\text{C4})$$

1064 Next, for the first and third terms on the left side of Eq. (C4),

$$u = \frac{1}{n} \frac{I_{ex}}{I_e^{1/2}} h^{2/3} \quad (C5)$$

1065

$$v = \frac{1}{n} \frac{I_{ey}}{I_e^{1/2}} h^{2/3} \quad (C6)$$

1066

$$\frac{\partial u}{\partial x} = \frac{\partial u}{\partial h} \frac{\partial h}{\partial x} + \frac{\partial u}{\partial I_{ex}} \frac{\partial I_{ex}}{\partial x} + \frac{\partial u}{\partial I_e} \frac{\partial I_e}{\partial x} = \frac{2}{3} \frac{u}{h} \frac{\partial h}{\partial x} + \frac{u}{I_{ex}} \frac{\partial I_{ex}}{\partial x} - \frac{1}{2} \frac{u}{I_e} \frac{\partial I_e}{\partial x} \quad (C7)$$

1067

$$\frac{\partial v}{\partial y} = \frac{\partial v}{\partial h} \frac{\partial h}{\partial y} + \frac{\partial v}{\partial I_{ey}} \frac{\partial I_{ey}}{\partial y} + \frac{\partial v}{\partial I_e} \frac{\partial I_e}{\partial y} = \frac{2}{3} \frac{v}{h} \frac{\partial h}{\partial y} + \frac{v}{I_{ey}} \frac{\partial I_{ey}}{\partial y} - \frac{1}{2} \frac{v}{I_e} \frac{\partial I_e}{\partial y} \quad (C8)$$

1068 After differentiating the composite function (Eq. (C7) and Eq. (C8)) using Man-
 1069 ning's flow velocity formula (Eq. (C5), Eq. (C6)), substituting it into Eq. (C4), and
 1070 rearranging $\partial h/\partial x$, the following equation is obtained.

$$\frac{\partial h}{\partial x} = -\frac{3}{5} \frac{h}{I_{ex}} \frac{\partial I_{ex}}{\partial x} + \frac{3}{10} \frac{h}{I_e} \frac{\partial I_e}{\partial x} - \frac{v}{u} \frac{\partial h}{\partial y} - \frac{3}{5} \frac{vh}{uI_{ey}} \frac{\partial I_{ey}}{\partial y} + \frac{3}{10} \frac{vh}{uI_e} \frac{\partial I_e}{\partial y} \quad (C9)$$

1071 Next, after substituting Eq. (C7) and the following Eq. (C10) into the first
 1072 and second terms of the equation of motion in the x direction for Eq. (C2), we get

$$\frac{\partial u}{\partial y} = \frac{\partial u}{\partial h} \frac{\partial h}{\partial y} + \frac{\partial u}{\partial I_{ex}} \frac{\partial I_{ex}}{\partial y} + \frac{\partial u}{\partial I_e} \frac{\partial I_e}{\partial y} = \frac{2}{3} \frac{u}{h} \frac{\partial h}{\partial y} + \frac{u}{I_{ex}} \frac{\partial I_{ex}}{\partial y} - \frac{1}{2} \frac{u}{I_e} \frac{\partial I_e}{\partial y} \quad (C10)$$

1073 After substituting Eq. (C9), which was organized earlier into Eq. (C11), we get

$$\begin{aligned} & \frac{2}{3} \frac{u^2}{gh} \frac{\partial h}{\partial x} + \frac{u^2}{gI_{ex}} \frac{\partial I_{ex}}{\partial x} - \frac{1}{2} \frac{u^2}{gI_e} \frac{\partial I_e}{\partial x} + \frac{2}{3} \frac{uv}{gh} \frac{\partial h}{\partial y} \\ & + \frac{uv}{gI_{ex}} \frac{\partial I_{ex}}{\partial y} - \frac{1}{2} \frac{uv}{gI_e} \frac{\partial I_e}{\partial y} + \frac{\partial z}{\partial x} + \frac{\partial h}{\partial x} + I_{ex} = 0 \end{aligned} \quad (C11)$$

1074 The following equation can be obtained by rearranging $v/uh/\partial y$.

$$\begin{aligned} & \frac{v}{u} \frac{\partial h}{\partial y} = \frac{3}{5I_{ex}} \left(\frac{u^2}{g} - h \right) \frac{\partial I_{ex}}{\partial x} + \frac{3}{10I_e} \left(-\frac{u^2}{g} + h \right) \frac{\partial I_e}{\partial x} \\ & + \frac{1}{5I_{ey}} \left(-\frac{2uv}{g} - \frac{3vh}{u} \right) \frac{\partial I_{ey}}{\partial y} + \frac{3}{10I_e} \left(-\frac{uv}{g} + \frac{vh}{u} \right) \frac{\partial I_e}{\partial y} + \frac{uv}{gI_{ex}} \frac{\partial I_{ex}}{\partial y} + \frac{\partial z}{\partial x} + I_{ex} \end{aligned} \quad (C12)$$

1075 After substituting Eq. (C12) into Eq. (C9) and rearranging it, the following $\partial h/\partial x$
 1076 is derived.

$$\frac{\partial h}{\partial x} = -\frac{\partial z}{\partial x} - I_{ex} - \frac{3}{5} \frac{u^2}{gI_{ex}} \frac{\partial I_{ex}}{\partial x} + \frac{3}{10} \frac{u^2}{gI_e} \frac{\partial I_e}{\partial x} + \frac{2}{5} \frac{uv}{gI_{ey}} \frac{\partial I_{ey}}{\partial y} + \frac{3}{10} \frac{uv}{gI_e} \frac{\partial I_e}{\partial y} - \frac{uv}{gI_{ex}} \frac{\partial I_{ex}}{\partial y} \quad (C13)$$

1077 By rearranging $\partial h/\partial y$ using the same process as before, the following equation
 1078 for $\partial h/\partial y$ is obtained.

$$\frac{\partial h}{\partial y} = -\frac{\partial z}{\partial y} - I_{ey} - \frac{3}{5} \frac{v^2}{gI_{ey}} \frac{\partial I_{ey}}{\partial y} + \frac{3}{10} \frac{v^2}{gI_e} \frac{\partial I_e}{\partial y} + \frac{2}{5} \frac{uv}{gI_{ex}} \frac{\partial I_{ex}}{\partial x} + \frac{3}{10} \frac{uv}{gI_e} \frac{\partial I_e}{\partial x} - \frac{uv}{gI_{ey}} \frac{\partial I_{ey}}{\partial x} \quad (C14)$$

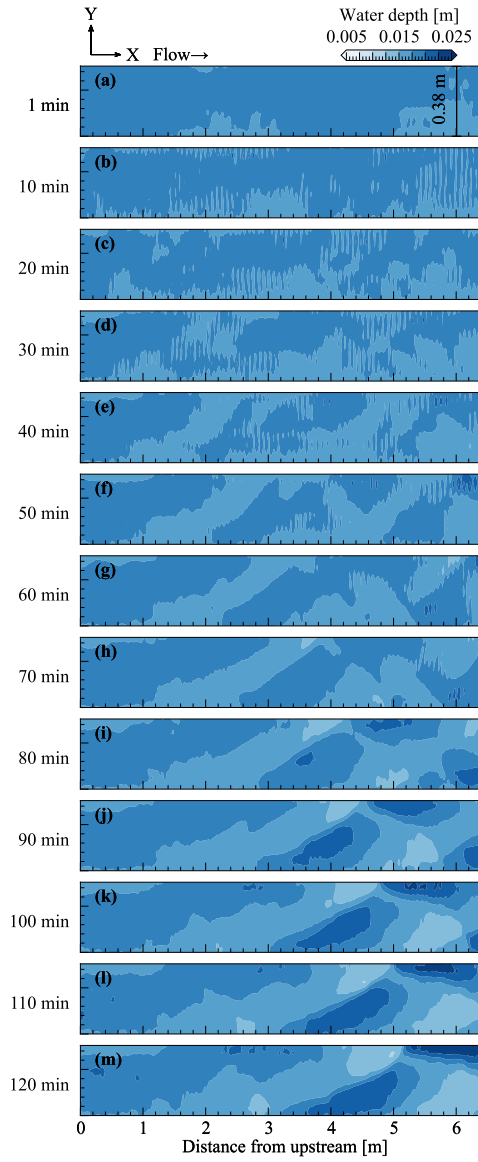


Figure 5. Temporal changes in the plan view for the observed water depth.

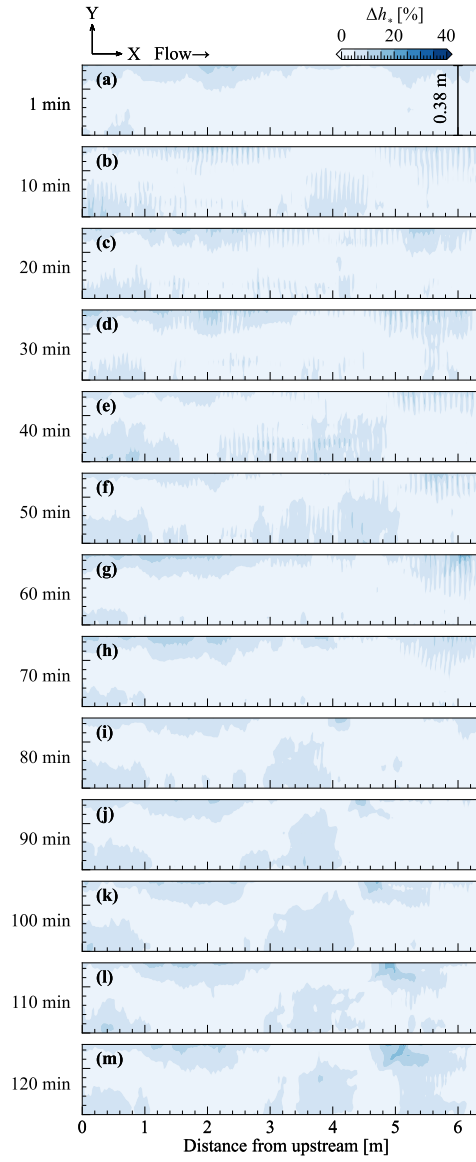


Figure 6. Difference between the measured and calculated values of the water depth that is made dimensionless using the measured value.

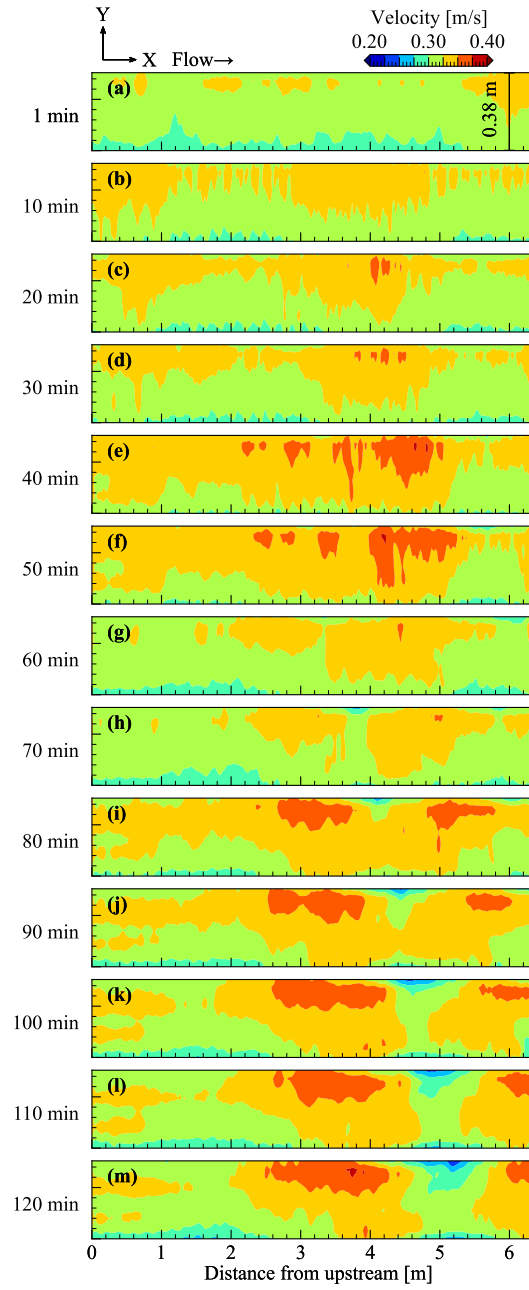


Figure 7. Temporal changes in the plan view for the calculated flow velocity.

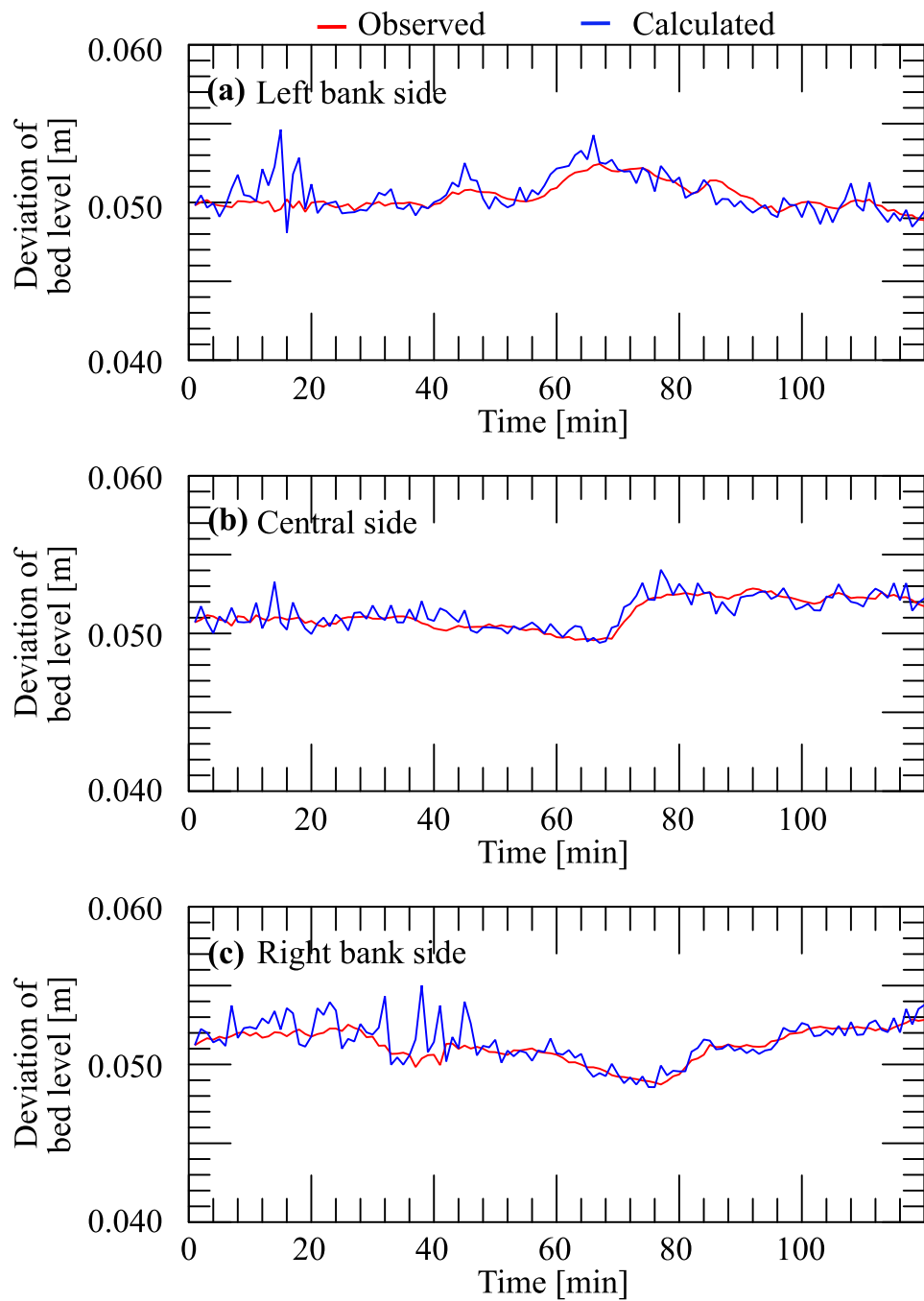


Figure 8. Bed-level time waveform: (a) Left bank side, (b) center, (c) right bank side.

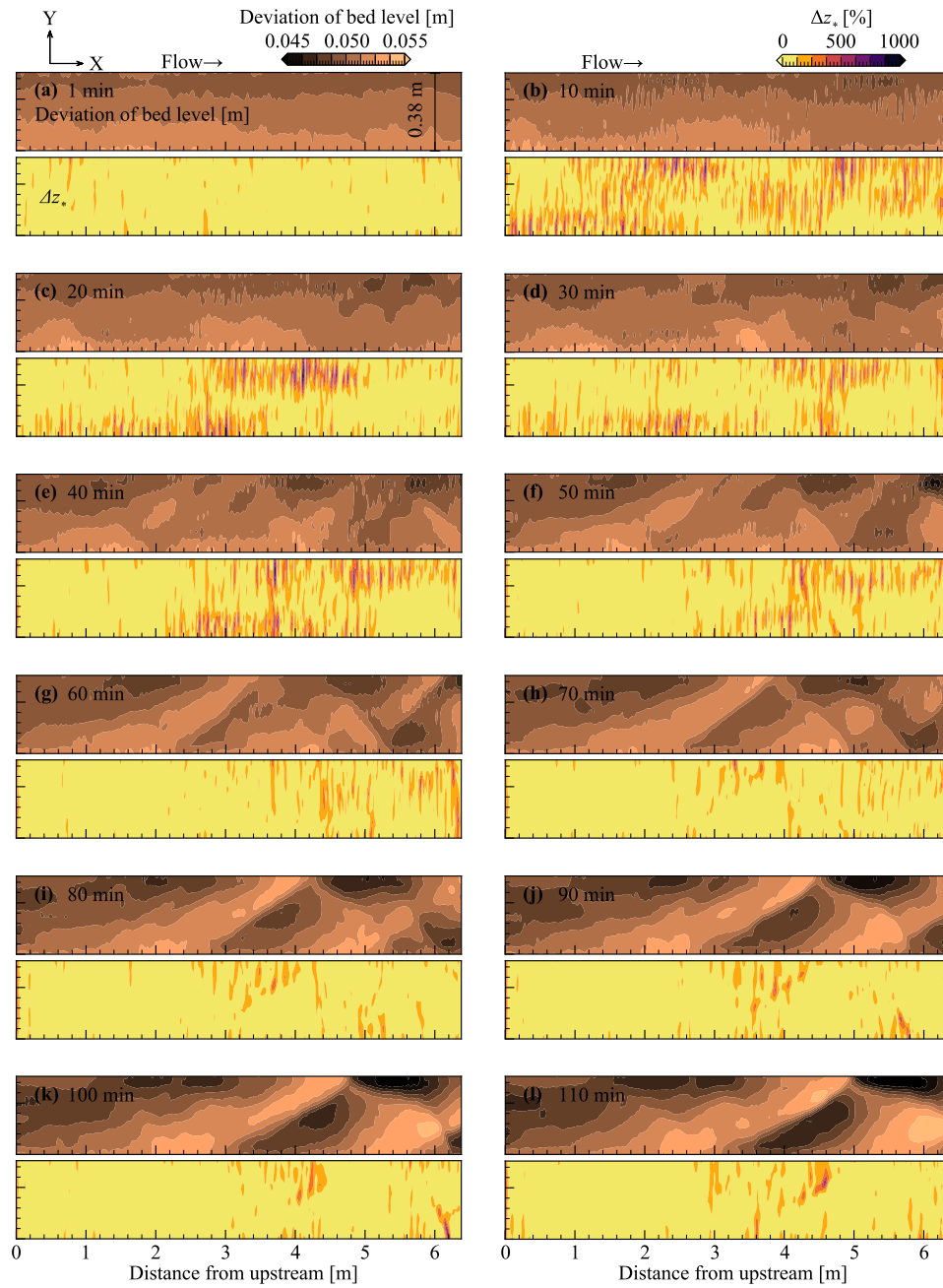


Figure 9. Temporal changes in the plan view for the observed bed topography and Δz_* .

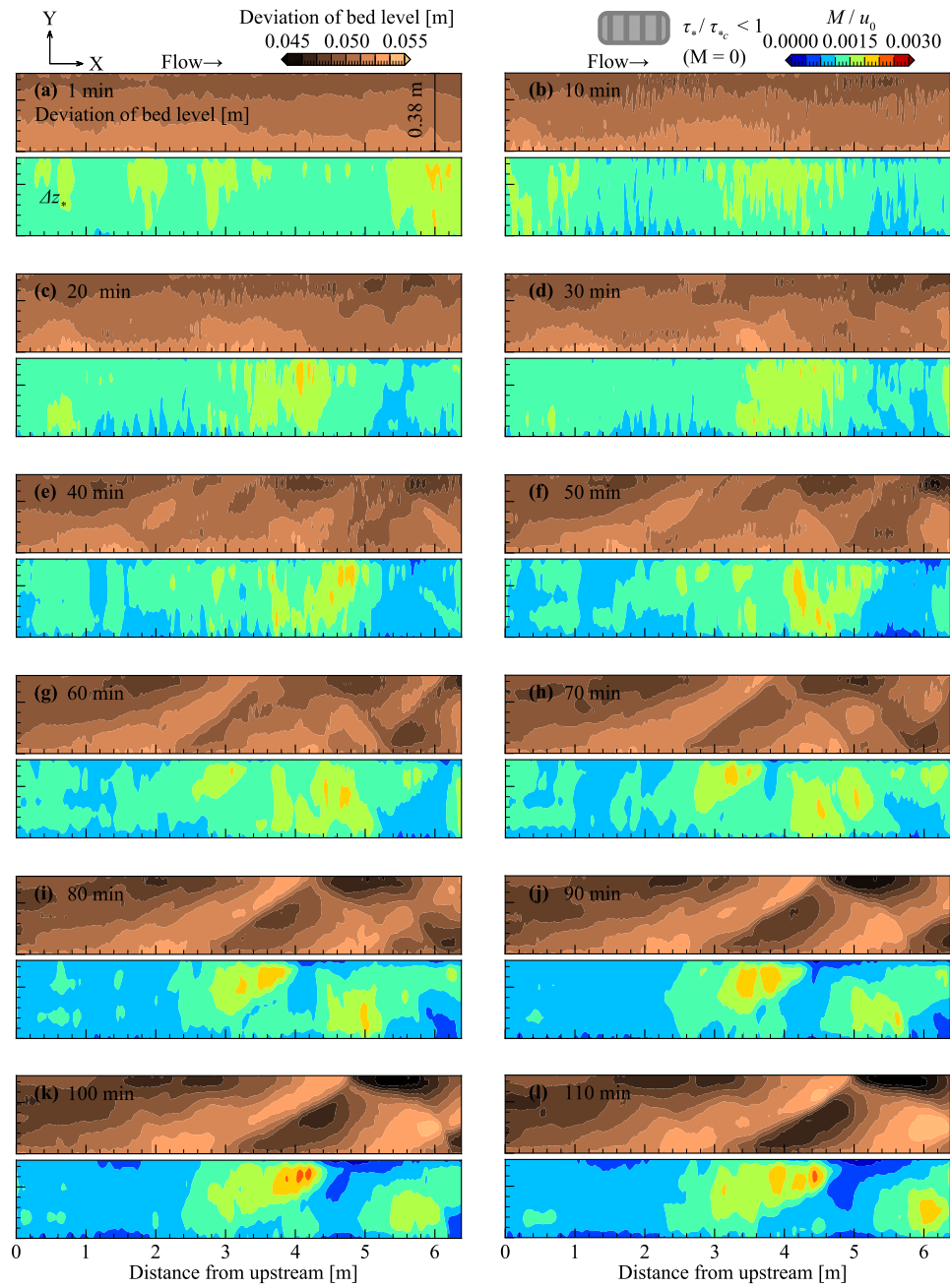


Figure 10. Temporal changes in the plan view for the observed bed topography and calculated migrating speed.

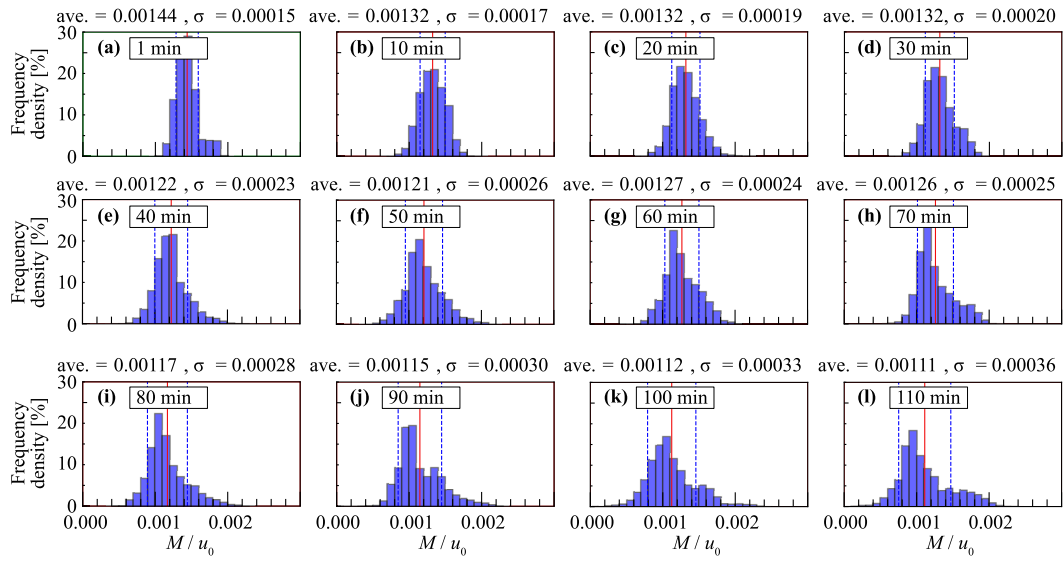


Figure 11. Histograms of migrating speed.

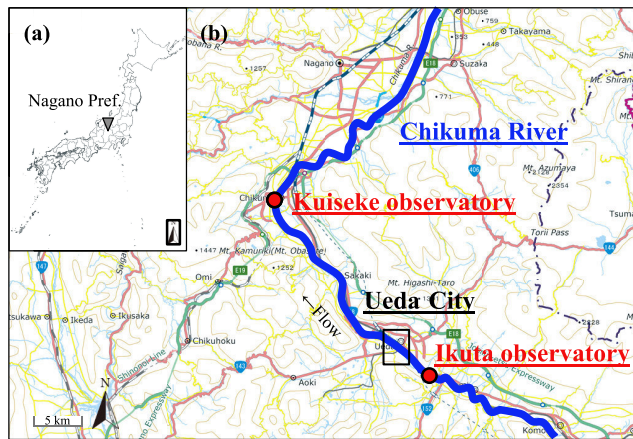


Figure 12. Overview of the study area: (a) geographic location, (b) map (GSI Maps (electronic land web) created by processing).

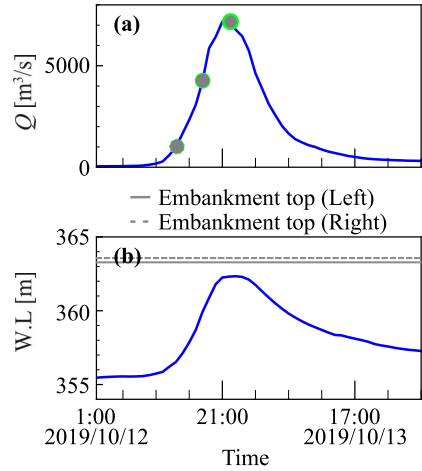


Figure 13. (a) Flow discharge hydrograph and (b) water level hydrograph.

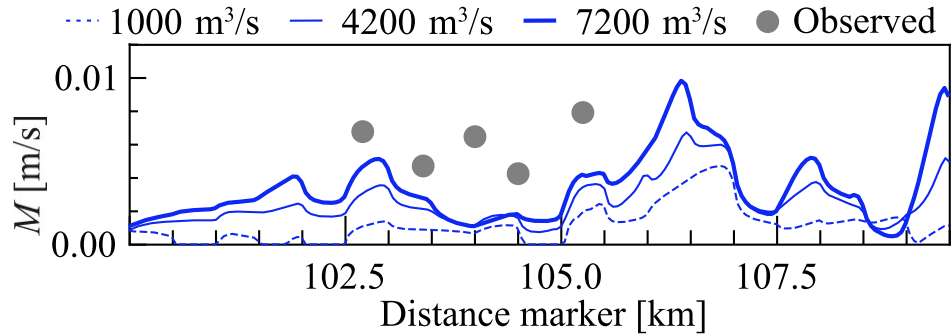


Figure 14. Calculated and measured values of migrating speed.

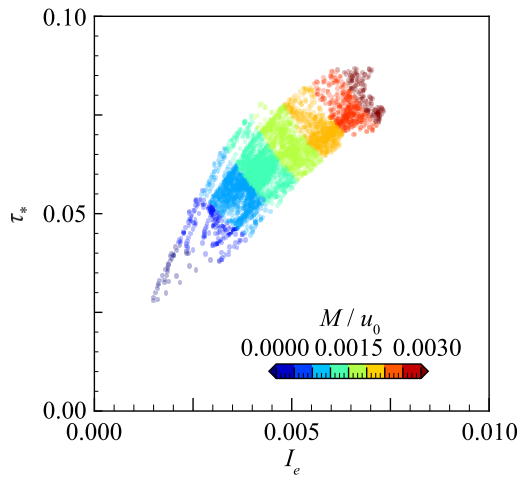


Figure 15. Relationship between energy slope, Shields number, and migrating speed.

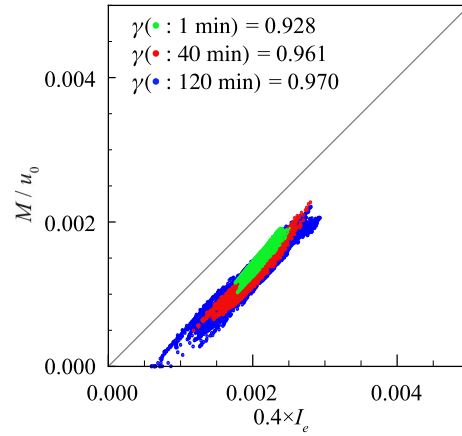


Figure 16. Relationship between migrating speed and energy slope.

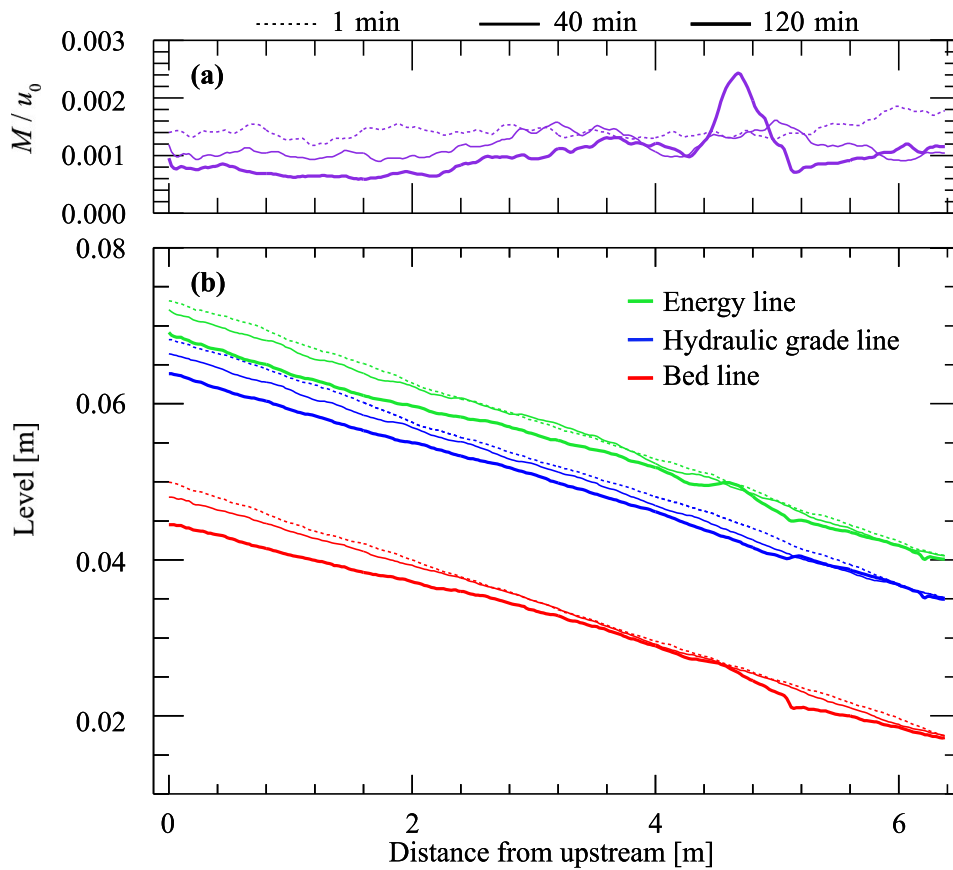


Figure 17. Longitudinal view of the (a) cross-sectional averaged migrating speed (b) and cross-sectional averaged bed level.

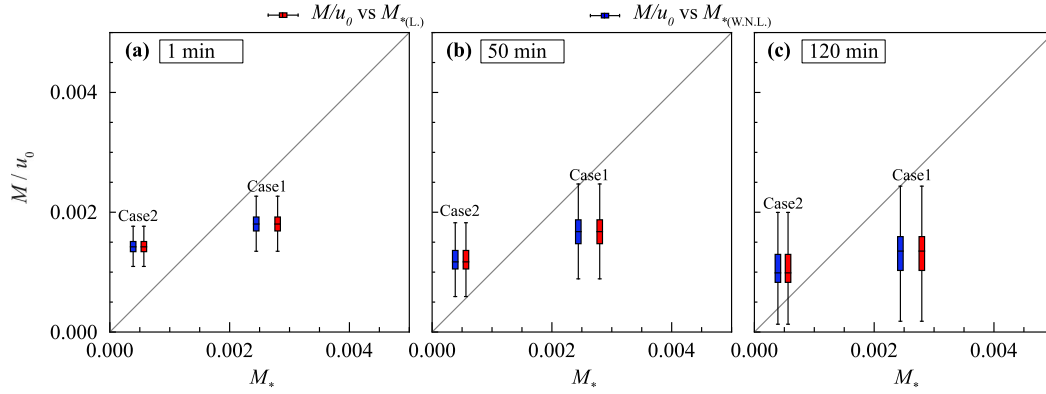


Figure 18. Relationship between migrating speed obtained by our method and migrating speed obtained by instability analysis.

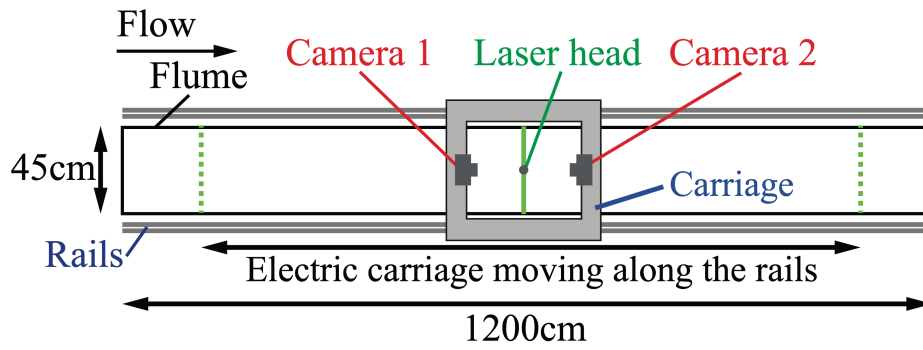


Figure A1. Plan view of the measuring device and flume.

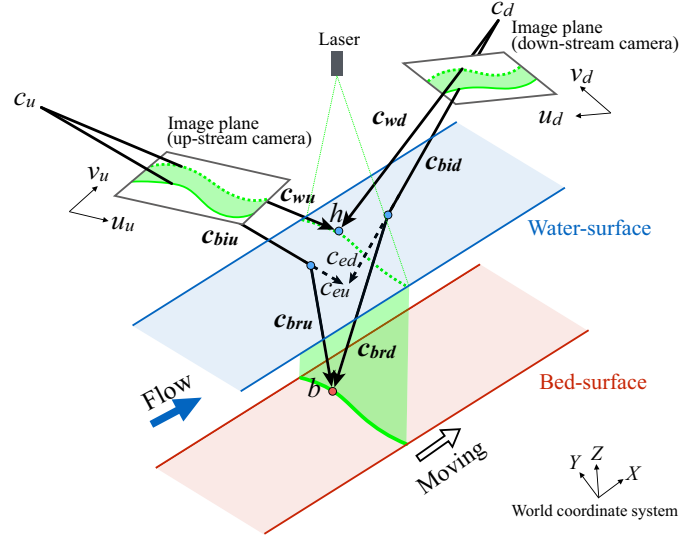


Figure A2. Outline of the geometric relations. C_u and C_d are the camera positions. h is calculated by observing the laser reflection on the water surface and is the intersection of the two observation vectors C_{wu} and C_{wd} . Reflection on the bed surface is observed at the position where it is refracted by the camera, $C_{biu} + C_{eu}(C_{bid} + C_{ed})$. By correcting the refracted reflection vector of the bed surface at the intersection point with the water surface, the observed vector of the bed surface becomes $C_{biu} + C_{bru}(C_{bid} + C_{brd})$.

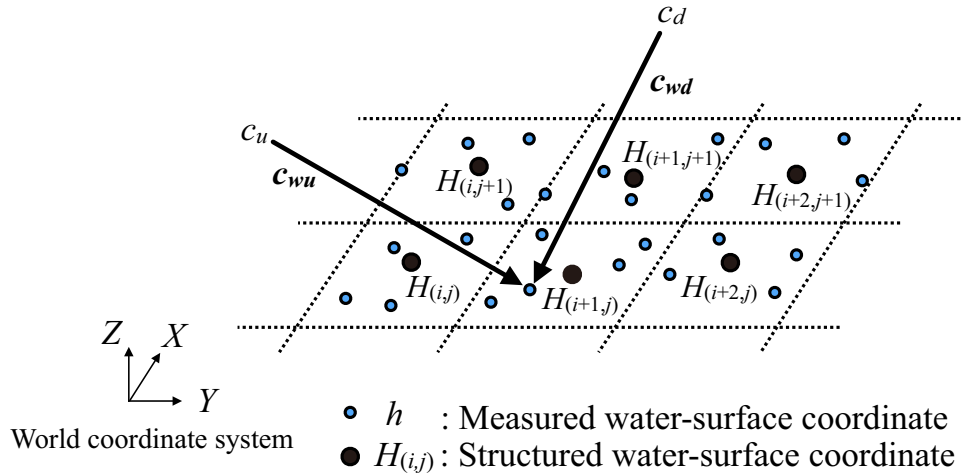


Figure A3. The structure-type function of the water level $H_{(i,j)}$, which is used for the refraction correction, is created from the calculated point cloud of h using the nearest point of the structure grid center coordinates.

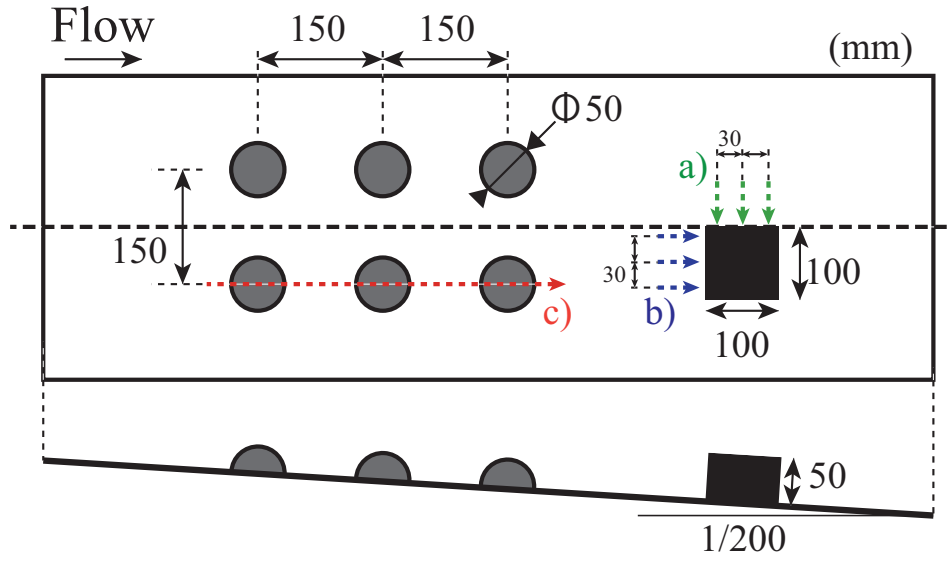


Figure A5. Arrangement of the objects of fixed-floor verification. The upper and lower panels show plan and cross-sectional views of the channel, respectively. The radius of the hemisphere is 25 mm, and the dimensions of the rectangle are 100×100×50 mm (width×length×height). The arrows in a) to c) indicate the measurement lines in the subsequent verification.

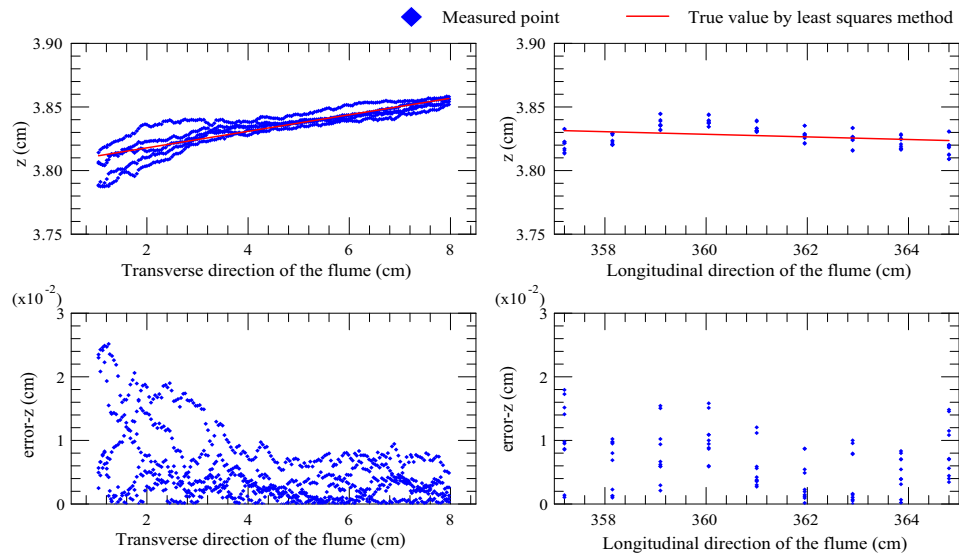


Figure A6. (Left) Upper figure shows the results of transverse measurements on the top surface of a rectangular area under dry conditions. Five measurements at 3-cm intervals in the longitudinal direction were superimposed by blue dots (15 sections in total). The red line is the estimated value obtained by the least-squares method and is regarded as the true value. The lower figure shows the z -error between the true and measured values. (Right) As in the left figure, the upper figure shows measurement results in the longitudinal direction. The results of five measurements at 3 cm in the transverse direction are superimposed.

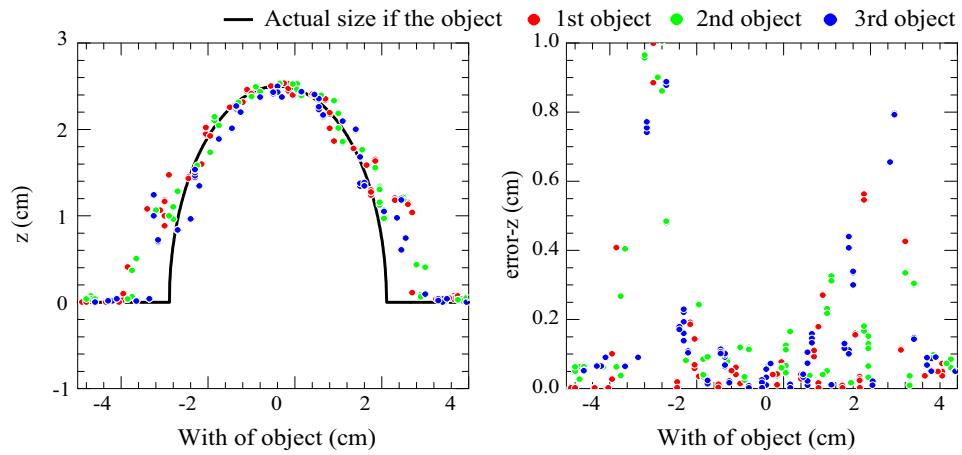


Figure A7. (Left) Results of five measurements in the longitudinal direction for three hemispheres on the right side under dry conditions are superimposed (15 sections in total). The measurement line was chosen to pass through the hemispherical center. The solid black line is the true value, which is a semicircle of radius 2.5 cm. (Right) The z -error between the true and measured values.

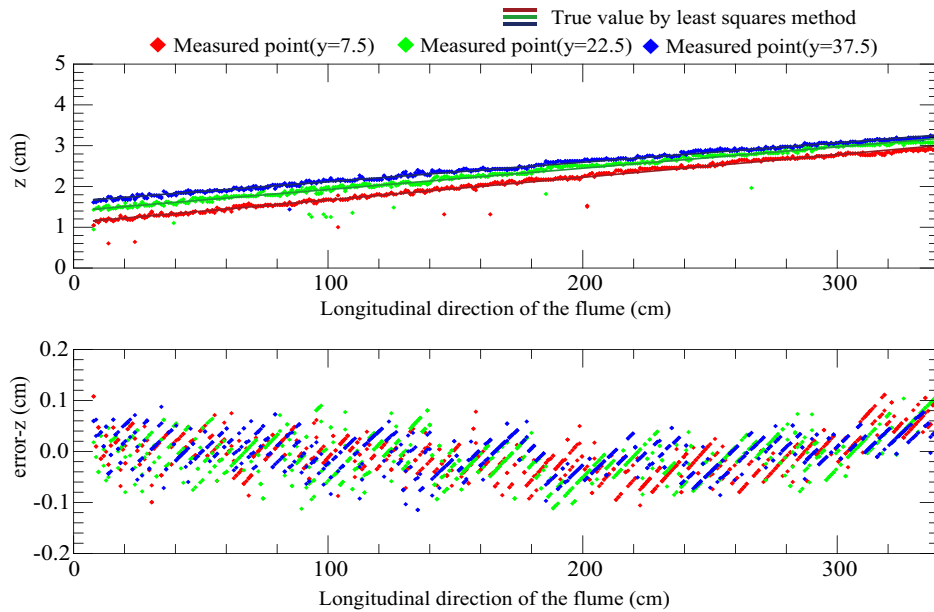


Figure A8. (Upper) Measurement results of the longitudinal section on the still water surface are shown for each measurement line, color-coded according to the distance from the starting point. The water depth increased longitudinally owing to the weir condition. The solid line of each color is the true value obtained using the least-squares method in each lateral direction. (Lower) The z -error between the true and measured values.

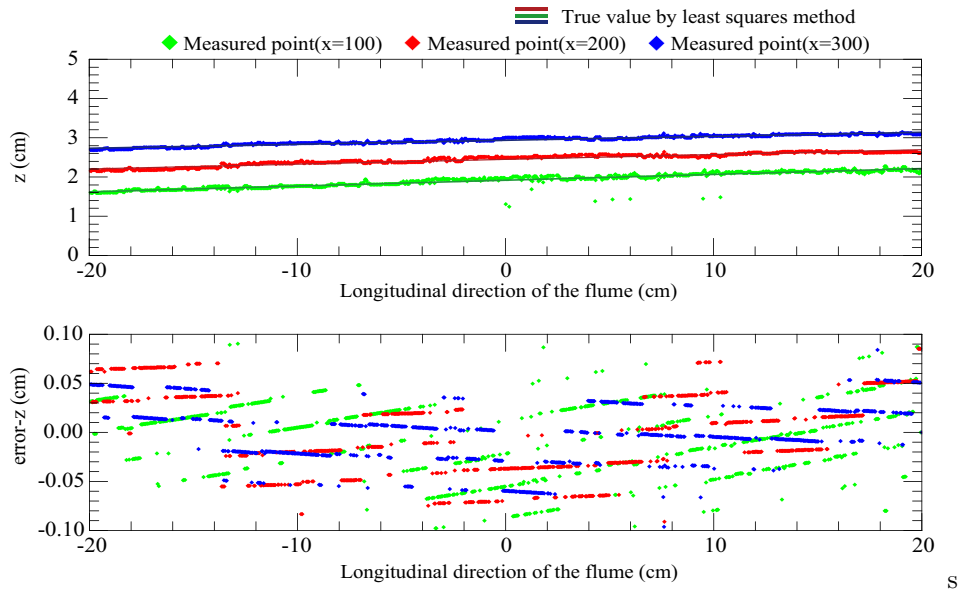


Figure A9. (Upper) Measurement results of the transverse section at the still water surface are shown by color-coding each measurement line according to the distance from the right bank. The solid line of each color is the true value obtained using the least-squares method for each lateral section. (Lower) The z -error between the true and measured values.

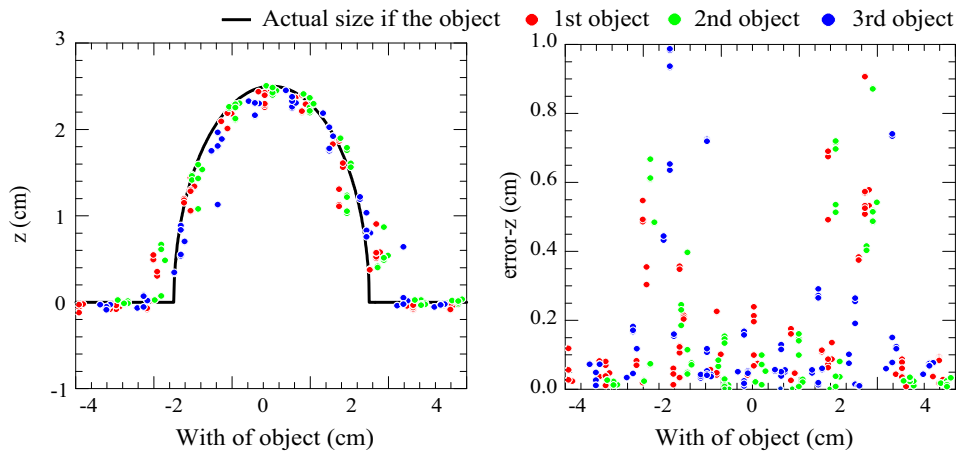


Figure A10. (Left) Results of five measurements in the longitudinal direction for the three hemispheres on the right side under still water conditions are superimposed (15 sections in total). The measurement line was chosen to pass through the hemispherical center. The solid black line is the true value, which is a semicircle of radius 2.5 cm. (Right) The z -error between the true and measured values.

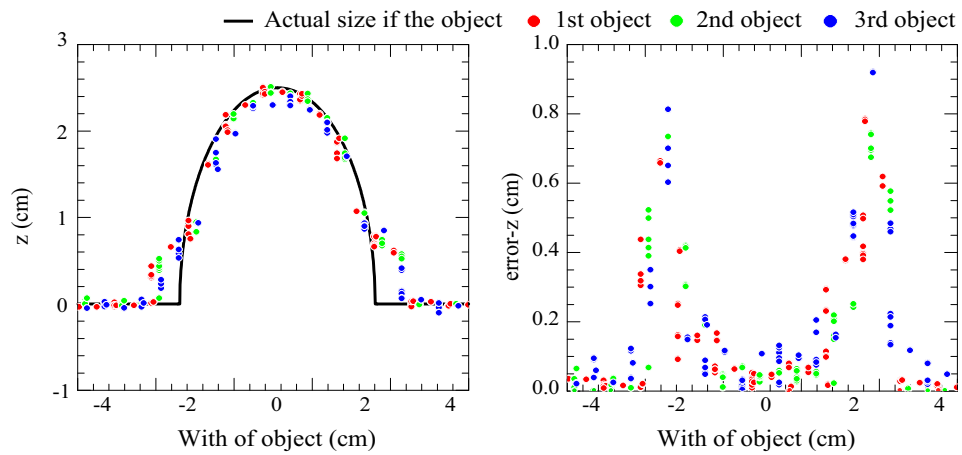


Figure A11. (Left) Results of five measurements in the longitudinal direction for the three hemispheres on the right side under flowing water conditions are superimposed (15 sections in total). The measurement line was chosen to pass through the hemispherical center. The solid black line is the true value, which is a semicircle of radius 2.5 cm. (Right) The z -error between the true and measured values.

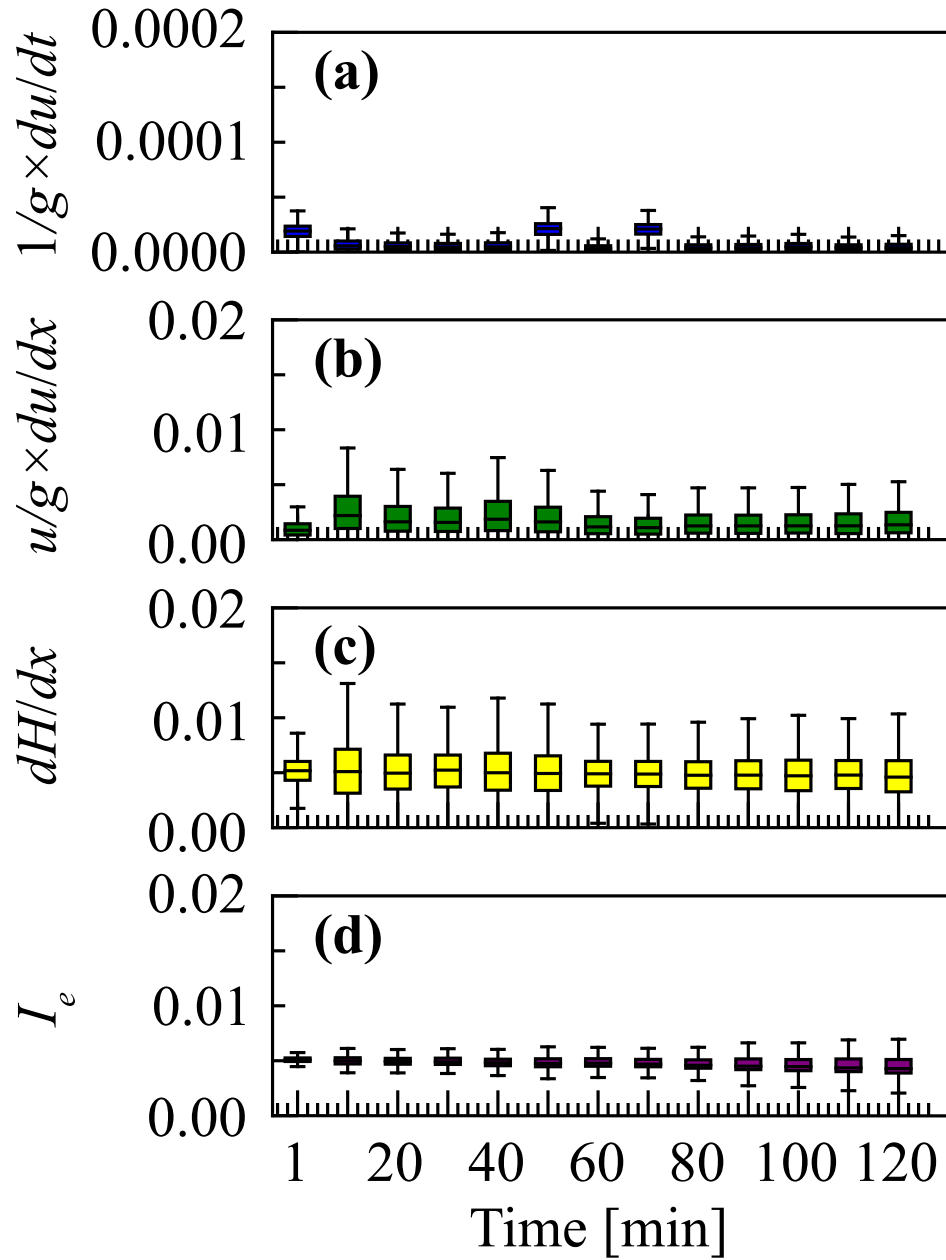


Figure B1. Temporal changes of the box plots for the (a) local term, (b) advection term, (c) pressure term, (d) and friction term.